



AMERICAN METEOROLOGICAL SOCIETY

Monthly Weather Review

EARLY ONLINE RELEASE

This is a preliminary PDF of the author-produced manuscript that has been peer-reviewed and accepted for publication. Since it is being posted so soon after acceptance, it has not yet been copyedited, formatted, or processed by AMS Publications. This preliminary version of the manuscript may be downloaded, distributed, and cited, but please be aware that there will be visual differences and possibly some content differences between this version and the final published version.

The DOI for this manuscript is doi: 10.1175/MWR-D-12-00343.1

The final published version of this manuscript will replace the preliminary version at the above DOI once it is available.

If you would like to cite this EOR in a separate work, please use the following full citation:

Adams-Selin, R., and R. Johnson, 2013: Examination of gravity waves associated with 13 March 2003 bow echo. *Mon. Wea. Rev.* doi:10.1175/MWR-D-12-00343.1, in press.



1 **Examination of gravity waves associated with 13 March 2003 bow echo**

2 Rebecca D. Adams-Selin⁺¹ and Richard H. Johnson⁺

3 ⁺Department of Atmospheric Science

4 Colorado State University

5 Fort Collins, Colorado

6 December 2012

7 (submitted to *Monthly Weather Review*)

¹Corresponding author address: Rebecca D. Adams-Selin, HQ Air Force Weather Agency 16th Weather Squadron, 101 Nelson Dr., Offutt AFB, NE, 68113. Email: rebecca.selin.ctr@offutt.af.mil

Abstract

8 Numerical simulations of the 13 March 2003 bow echo over Oklahoma are used to eval-
9 uate bow echo development and its relationship with gravity wave generation. Multiple
10 fast-moving (with speeds of 30-35 m s⁻¹) gravity waves are generated in association with
11 fluctuations in the first vertical mode of heating in the convective line. The surface impacts
12 of four such waves are observed in Oklahoma mesonet data during this case. Observations of
13 surface pressure surges ahead of convective lines prior to the bowing process are reproduced;
14 a slower gravity wave produced in the simulation is responsible for a pre-bowing pressure
15 surge. This slower gravity wave, moving at approximately 11 m s⁻¹, is generated by an in-
16 crease in low-level microphysical cooling associated with an increase in rear-to-front flow and
17 low-level downdrafts shortly before bowing. The wave moves ahead of the convective line and
18 is manifested at the surface by a positive pressure surge. The pattern of low-level vertical
19 motion associated with this wave, in conjunction with higher-frequency gravity waves gener-
20 ated by multicellularity of the convective line, increases the immediate pre-system CAPE by
21 approximately 250 J kg⁻¹ just ahead of the bowing segment of the convective line. Increased
22 pre-system CAPE aids convective updraft strength in that segment despite amplified updraft
23 tilt due to a stronger cold pool and surface-based rear-to-front flow, compared to updraft
24 strength in other, non-bowing segments of the convective line.

25 **1. Introduction**

26 The ability of convective systems to generate gravity waves is well-documented in the lit-
 27 erature (Nicholls et al. 1987; Bretherton and Smolarkiewicz 1989; Schmidt and Cotton 1990;
 28 Mapes 1993; Fovell 2002, 2006; Knupp 2006). Specifically, changes in heating and cooling
 29 rates in the atmosphere, as are often found with convection, can result in the generation of
 30 gravity waves due to the difference in buoyancy between the convection and the surrounding
 31 environment (Bretherton and Smolarkiewicz 1989; Nicholls et al. 1991; Mapes 1993). If the
 32 vertical heating profile is a harmonic of the depth of the troposphere, the partial reflection
 33 of the wave energy at the tropopause allows hydrostatic waves to propagate horizontally for
 34 large distances without the aid of a trapping level other than the tropopause (Nicholls et
 35 al. 1991). The label of such a wave is equal to the number of antinodes in the heating profile
 36 that generates it; for example a $n = 1$ mode wave is generated by a heating profile that
 37 extends throughout the troposphere with its maximum at mid-levels.

38 This type of vertical diabatic heating profile is typical during the formation of a convective
 39 line due to the latent heat release from condensation, freezing, and deposition in the updraft
 40 (Houze 1982; Johnson and Young 1983; Gallus and Johnson 1991). The speed of these low
 41 frequency waves is given by:

$$42 \quad c = \frac{NH}{n\pi} \quad (1)$$

43 where N is the Brunt-Väisälä frequency, H is the vertical depth of the atmosphere, and n is
 44 the vertical mode of the heating profile (Nicholls et al. 1991). In this study, the N used is
 45 the N_m defined in Bryan and Rotunno (2009). For subsaturated air, N_m is defined as

$$46 \quad \left(\frac{g}{\theta_v} \right) \frac{\partial \theta_v}{\partial z} \quad (2)$$

47 where g is gravitational acceleration, z height, $\theta_v = \theta(1 + q_v R_v / R_d) / (1 + q_v + q_l)$, q_v and q_l
 48 the water vapor and liquid water mixing ratios, and R_d and R_v the gas constants for dry air
 49 and water vapor, respectively. The full description of N_m for saturated air is given in Bryan
 50 and Rotunno (2009). Typical values of N (0.01 s^{-1}) and H (10 km) yield a $n = 1$ wave

51 speed of approximately 30 m s^{-1} .

52 Nicholls et al. (1991) calculated the linear atmospheric response to the introduction of
53 a $n = 1$ warming temperature profile (Figs. 1a-d). In that study, the heat source, located
54 at $x=0 \text{ km}$, was turned on immediately at the start of the solution, left on for 2 hours, and
55 then turned off. The switch “on” of the heat resulted in a temporary low (high) pressure
56 perturbation at the surface (aloft), along with an increase in the u wind flow toward the
57 heating source at lower levels, and away from the heating source at upper levels (at $x=450 \text{ km}$
58 in Figs. 1a, c; also noted by Mapes 1993). An increase in potential temperature particularly
59 at mid-levels also occurs, generated by subsidence throughout the column following passage
60 of the first wave front (Figs. 1b, d). At the surface, this appears as a temporary decrease
61 in pressure unaccompanied by a change in temperature. When the heating ceases, a second
62 signal travels at the same speed away from the system. This second response contains ascent
63 throughout the column, and the pressure, potential temperature, and u wind fields return
64 to the ambient values (Figs. 1a-d at $x=225 \text{ km}$).

65 Within the idealized analytical solution of Nicholls et al. (1991), the ambient environment
66 returns to its initial state after both responses pass. However, it was noted by Mapes
67 (1993) that the pre-storm environment is in a sense permanently modified in respect to the
68 convective system, as the second response doesn’t appear until the system, and its associated
69 heating, dissipates. The subsidence-induced slight warming and drying throughout the depth
70 of the atmosphere resulting from the first response is a permanent modification, particularly
71 in the mid-levels.

72 The heating profile generated by a system’s stratiform precipitation region, of $n = 2$ or
73 even $n = 3$ structure consisting partially of cooling in low levels, can generate yet another
74 low-frequency gravity wave (Nicholls et al. 1991; Mapes 1993; Lane and Reeder 2001; Fovell
75 2002; Fovell et al. 2006). In the $n = 2$ wave, upward (downward) motion is excited on the
76 leading edge of the wave throughout the lower (upper) half of the troposphere; the lower half
77 of the troposphere is adiabatically cooled (Figs. 1f, h at approximately $x=120 \text{ km}$ displays

78 the combined $n = 1$ and 2 wave responses). The wind profile is modified to create mid-
79 tropospheric inflow (Fig. 1e, Fovell 2002); a mid-tropospheric low pressure perturbation is
80 created as well, with high pressure perturbations generated in the lowest and highest third
81 of the troposphere (Fig. 1g). Through (1), it can be seen that this wave moves at half the
82 speed of the $n = 1$ wave. Pandya and Durran (1996) and Pandya et al. (2000) found that
83 the wind perturbations generated by the combination of $n = 1$ and 2 gravity waves could
84 largely explain the circulations within a squall line, including the onset of rear-to-front flow.

85 The $n = 3$ wave also exhibits a lifting and cooling response on its leading edge, but
86 over the lowest one-third of the atmosphere (Lane and Reeder 2001). The $n = 3$ cooling
87 profile is typically associated with the onset of melting contributing to a low-level cooling
88 maximum. While both $n = 2$ and $n = 3$ wave modes cool and moisten the lower levels, Lane
89 and Reeder (2001) found that the $n = 3$ wave had a more significant effect in decreasing
90 the pre-storm environment convective inhibition (CIN). This is because the peak upward
91 vertical motions associated with this wave were located lower, closer to the sub-cloud layer,
92 a major determinant of CIN. Combinations of the $n = 2$ and $n = 3$ waves can act as positive
93 feedbacks to their generating systems, cooling and moistening the lower level air feeding
94 into the storm and organizing surrounding convection (Schmidt and Cotton 1990; Mapes
95 1993; McAnelly et al. 1997; Lane and Reeder 2001; Fovell 2002; Fovell et al. 2006; Lane and
96 Moncrieff 2008; Bryan and Parker 2010; Lane and Zhang 2011).

97 Heating profiles that are not harmonics of the depth of the troposphere also generate
98 gravity wave responses similar in appearance to those discussed above. With reduced op-
99 portunity for reflection these waves can propagate vertically out of the troposphere more
100 quickly, but that is not always the case: gravity wave responses to low-level cooling were
101 produced in Parker (2008) and Schumacher (2009) that remained near the surface. In ideal-
102 ized linear simulations by Haertel and Johnson (2000), they found the gravity wave response
103 to cooling over the lowest 4 km of the troposphere results in a prominent pressure signal at
104 the surface 6 hours into the simulation. This response was in addition to the features associ-

105 ated with the also-generated gravity current. Furthermore, if the cooling source moves at a
106 speed approximately equal to that of its generated wave, the wave response is amplified. For
107 example, the positive surface pressure perturbation was from 20 to 35% larger in magnitude
108 when the cooling source moved at a speed close to the gravity wave speed as opposed to
109 remaining stationary.

110 Finally, Fovell et al. (2006) noted that high-frequency, non-hydrostatic gravity waves
111 propagating in the troposphere ahead of a squall line can be generated by multicellular
112 development and frequent temporal changes of the heating profile within a convective line.
113 These waves do require a trapping layer to not quickly propagate out of the troposphere; the
114 curvature of the wind profile due to outflow aloft from the system at anvil level can provide
115 this. They found that small amounts of water condensed within the updrafts associated with
116 these high-frequency waves, increasing the parcel's buoyancy, and small clouds formed. This
117 particularly can occur if the lower levels have previously been lifted, cooled, and moistened
118 by a low-frequency gravity wave. The newly formed clouds are then advected toward the
119 main system by the system-relative wind. As the clouds are ingested by the system, the
120 increase in buoyancy can act to locally strengthen the convective line, provided the cloud
121 has not already developed rainfall and its own associated cold pool (Fovell et al. 2006).

122 Few studies have documented real-world observations of hydrostatic waves. Bryan and
123 Parker (2010) observed buoyancy and pressure patterns in conjunction with an Oklahoma
124 squall line that appeared to be a $n = 1$ gravity wave. Adams-Selin and Johnson (2010, here-
125 after ASJ10) noted surface pressure and temperature patterns associated with an Oklahoma
126 bow echo that appeared to correspond to $n = 1$ and 2 gravity waves, but because that study
127 only dealt with surface observations, this could not be confirmed. One specific pressure
128 feature observed by ASJ10, a surge of the mesohigh partially ahead of the convective line,
129 appeared in conjunction with new bowing in 35 of 39 bow echoes observed in Oklahoma over
130 the 4-year ASJ10 study, suggesting a connection to bowing development.

131 Thus, the goal of this study is to determine if the surface pressure features noted in

132 ASJ10 were indeed generated by gravity waves, and if so to ascertain the effect of those
133 waves on the bow echo system particularly in relation to new bowing development. An
134 idealized, high resolution Cloud Model 1 simulation (CM1, Bryan and Fritsch 2002) will be
135 used to reproduce these pressure features and their cause. A discussion of the bow echo,
136 which occurred on 13 March 2003, and all observed pressure features is given in Section 2.
137 The CM1 model used is described in Section 3. Sections 4 and 5 analyze the low-frequency
138 wave features simulated in the CM1 model, while Section 6 discusses the high-frequency
139 wave features seen. Section 7 provides the conclusions.

140 **2. 13 March 2003 case review**

141 *a. Fast-moving low pressure perturbations*

142 Figure 2, from ASJ10, displays composite WSI NOWrad radar reflectivity data, overlaid
143 with high-pass Lanczos-filtered pressure and temperature data from the Oklahoma Mesonet.
144 (The high-pass filtering was designed to remove synoptic features from the data; see ASJ10
145 for more details.) The 13 March 2003 bow echo initialized as a convective line in central
146 Oklahoma, in isolation from other convection at 0230 UTC (Fig. 2a). A low pressure region
147 was evident centered over the convective line. This low pressure region quickly split and
148 propagated away from the convective line (0345 UTC, Fig. 2b).

149 Data timeseries from Oklahoma Mesonet stations VANO and HUGO, the locations of
150 which are shown by black dots in Fig. 2a, are given in Fig. 3. A dip in pressure, unac-
151 companied by a temperature change, is shown at arrow [a] at both stations. This would
152 seem to be indicative of a $n = 1$ gravity wave feature, as discussed above. In ASJ10, this
153 dip in pressure was tracked in numerous Mesonet stations across Oklahoma, and an average
154 ground-relative speed of 34.1 m s^{-1} was calculated. Isochrones of this feature are displayed
155 in Fig. 4a. The mean environmental tropospheric wind speed parallel to the direction of
156 motion of the feature, 1.6 m s^{-1} , was computed using the 0000 UTC sounding from Norman,
157 Oklahoma (KOUN, Fig. 5). Accounting for this tailwind yielded an actual feature speed of
158 32.5 m s^{-1} .

159 Upon further examination of these timeseries, additional pressure features, also possibly
160 indicative of gravity waves, were noted. Because these features are such small variations in
161 pressure, they did not appear in the objective analysis. However, in Fig. 3, arrows [b], [c],
162 and [d] at each station are also pressure rises and dips unaccompanied by surface temperature
163 changes. These features were evident at multiple Mesonet stations across Oklahoma as well,
164 and isochrones of each feature are shown in Figs. 4b, c, and d. The ground-relative speeds
165 of these features are estimated to be 32.8, 28.3, and 35.5 m s⁻¹, which are very similar to
166 the ground-relative speed of the initial feature denoted by arrow [a], particularly considering
167 the possible errors inherent in the estimation.

168 As discussed above, Nicholls et al. (1991) noted that upon the decrease of the amplitude
169 of a $n = 1$ heating profile, a positive pressure perturbation propagates quickly away from
170 the heating source in the lower half of the troposphere. Thus, it is possible that the low
171 pressure perturbations indicated by arrows [a] and [c] were gravity waves generated by a
172 sudden increase in the amplitude of a $n = 1$ heating profile, and the pressure increases at
173 arrows [b] and [d] signatures of a sudden decrease in that profile. The large magnitude of
174 the pressure response at [a] could have resulted from the larger, initial increase in convective
175 heating as the updraft first developed. However, without observations of the heating profile
176 within the convective system, such suppositions cannot be validated.

177 Bryan and Parker (2010) observed similar oscillations in surface pressure prior to passage
178 of a squall line. They related the initial oscillation in surface pressure to the combination
179 of an approaching cold front and a hydrostatic response to surface cooling by anvil shading.
180 In this case the synoptic features have been removed from the pressure data by the filtering
181 technique, and the anvil had not yet reached the stations when the pressure rises at [b]
182 and [d] occurred. Nevertheless, determination of the features as gravity waves requires a
183 numerical model.

184 *b. Pressure surge*

185 The second pressure feature associated with the system noted by ASJ10 was a mesohigh

186 surge partially ahead of the convective line. Between 0345 and 0515 UTC (Figs. 2b, c) a
187 mesohigh pressure perturbation formed over the convective line and spread southwestward as
188 the convective intensity strengthened. At 0545 UTC (Fig. 2d) the mesohigh surged partially
189 ahead of the convective line. This was shortly followed by new bowing development within
190 the line at 0615 UTC (Fig. 2e).

191 It was noted in ASJ10 that the size of the mesohigh pressure surge in this figure produced
192 by the objective analysis was excessive compared to timeseries observations. Given the
193 pressure surge speed of 21.6 m s^{-1} during this time, the distance corresponding to the
194 20-min interval between the initial pressure rise and final pressure peak at station VANO
195 (arrows [e] and [f] in Fig. 3a) should be 25.9 km. However, the pressure interval in Fig. 2d is
196 approximately 60 km. Thus, while the mesohigh surge ahead of the convective line existed,
197 its size was overestimated by about a factor of two to three. Multiple objective analysis
198 methods were tried in an attempt to fix this overestimation, but it was an inherent problem
199 in all analysis methods.

200 Figure 3a shows a sharp increase in pressure, a wind shift of almost 180 degrees, and
201 an increase in wind speed all at 0535 UTC (arrow [e]), but no accompanying potential
202 temperature drop. The sharp temperature drop and onset of rain twenty minutes later at
203 0555 UTC (arrow [f]) indicated the arrival of the surface cold pool or gravity current. This
204 pressure rise, significantly in advance of the temperature drop, occurred at almost all Mesonet
205 stations passed by the bow echo system, including station HUGO (Fig. 3b, arrows [e] and
206 [f].) The ground-relative speed of the feature was estimated to be 21.6 m s^{-1} (ASJ10). If the
207 mean environmental wind speed of 1.6 m s^{-1} in the direction of surge motion is accounted
208 for, the actual feature speed is 20.0 m s^{-1} .

209 These observations could be indicative of one of three features: a gravity wave response
210 generated by low-level cooling behind the convective line, similar to simulations in Haertel et
211 al. (2001); a non-hydrostatic pressure response to an intensifying cold pool as in Wakimoto
212 (1982) or Klemp (1994); or a bore propagating ahead of the system in a stable boundary layer

213 as in Parker (2008). Without observations above the surface it is not possible to discriminate
214 among these three possibilities. Thus, a numerical model was used to simulate and evaluate
215 this feature.

216 3. Model description

217 Cloud Model 1 (CM1, Bryan and Fritsch 2002), version 1.15, was initialized with the
218 0000 UTC 13 March 2003 Norman, Oklahoma (KOUN) sounding, which is shown in Fig. 5.
219 This sounding was released approximately two hours prior to convective initiation, and
220 100 km to the south. Minor smoothing was performed to remove absolute instabilities
221 and prevent overturning immediately after initialization, and missing moisture data were
222 extrapolated to upper levels, but otherwise the sounding was unmodified. The observed
223 convection formed along a southwest-northeast line approximately 60° clockwise of the north-
224 south direction (Fig. 2a). The wind profile from the sounding was used unmodified in the
225 idealized simulation, but the idealized convection initiated along a south-north line. As a
226 result, the simulated line-normal wind shear values were different than those of the observed
227 convective line. The 0-2.5 km shear in the simulation was 14 m s^{-1} instead of the observed
228 11.7 m s^{-1} , and 0-5 km shear was 14.2 m s^{-1} instead of 6 m s^{-1} .

229 In a WRF simulation of this case study, the 0-5 km wind shear at KOUN at the time of
230 convective initialization had increased to 9 m s^{-1} , suggesting that the environmental shear
231 was increasing after the 00 UTC sounding. In an idealized simulation with the initial wind
232 direction at each point rotated by 60° counter-clockwise so the line-normal shear values were
233 identical to those observed, a bow echo did not form, suggesting shear over a deeper layer
234 may be necessary for formation of an intense convective line as in Stensrud et al. (2005). A
235 discussion of these implications, however, is beyond the scope of this study.

236 The domain covered 300 km (x direction) by 200 km (y direction) by 18 km vertically.
237 A horizontal resolution of 250 m was used with a 2 s time step. The vertical resolution was
238 100 m from the surface to 4 km aloft; the resolution stretched to 500 m above 8 km. Lateral
239 boundary conditions were open-radiative; lower and upper boundary conditions were zero-

240 flux. Vertically implicit Klemp-Wilhelmson time-splitting was used with an acoustic time
241 step of 1/3 s. Rayleigh damping was applied above 14 km with an inverse e-folding time
242 of 1/300 s⁻¹. The Thompson et al. (2008) microphysics parameterization and a prognostic
243 TKE subgrid turbulence parameterization (Bryan and Fritsch 2002) were used; radiation
244 and surface flux parameterizations were not included. The domain was translated 12.5 m
245 s⁻¹ in the x direction and 3.3 m s⁻¹ in the y direction to keep the system inside.

246 The initialization method was the “cold pool-dam break” (Weisman et al. 1997). In this
247 method, a “cold dam” of air was created along the left side of the domain by decreasing the
248 initial potential temperature. This was done from 0 to 100 km in the x direction, and 30 to
249 170 km in the y direction. The magnitude of the potential temperature perturbation was -6
250 K at the surface, and linearly decreased until reaching 0 K 2.5 km aloft. As the simulation
251 began, the cold pool dam “broke” and surged forward as a gravity current. Air in advance
252 of the gravity current was forced upward, generating convection.

253 Coriolis forcing was not included in this simulation. Previous studies have noted that
254 the temperature perturbations generated by gravity waves become trapped within a Rossby
255 deformation radius, dependent upon the speed of the gravity wave (Johnson and Mapes 2001;
256 Liu and Moncrieff 2004). The time and space scales within this study are small enough that
257 this does not affect the results. However, these effects would begin to be noticed when
258 tracking a fast-moving gravity wave over larger spatial scales; for a gravity wave at the
259 latitude of Oklahoma, the Rossby radius of deformation (given as $\lambda_R = NH/f_c$, where f_c
260 is the Coriolis parameter at 35 ° N latitude, and H the height of the troposphere, 12 km)
261 would be approximately 1120 km.

262 **4. Multiple $n = 1$ gravity waves**

263 Within the CM1 simulation, convection initializes at 0:15 (15 minutes) simulation time,
264 directly over the edge of the gravity current created by the broken “cold pool dam”. By
265 0:35 cloud water reaches approximately 12 km vertically, and remains there for the rest of
266 the simulation. A low pressure perturbation (defined as departure from the initial pressure

267 field) of -1 hPa becomes evident at the lowest model level parallel to and just ahead of the
268 convective line (not shown). By 0:50, this feature has propagated approximately 30 km
269 ahead of the convective line (Fig. 6a), and appears very similar to the observed fast-moving
270 low pressure perturbation noted in Figs. 2a and b.

271 The vertical structure of this low pressure anomaly is displayed in Fig. 7. At simulation
272 time 0:50, in Figs. 7a and b, it is located at approximately $x=130$ km, where a low pressure
273 perturbation in the lower half of the atmosphere is overlaid by a high pressure perturbation
274 aloft. (The convective line is at 105 km.) Subsidence is indicated in the “eastern” half of the
275 low pressure anomaly, and ascending motion in the “western” half. A temporary warming
276 in the potential temperature field (Fig. 7b) is colocated with the pressure perturbations, due
277 to the adiabatic warming and cooling associated with the downdraft-updraft couplet. The
278 environmental flow toward the system is strengthened from the surface to 6 km aloft, and
279 the flow away from the system is also intensified, at 6 km and above (Fig. 7b). In sum,
280 this feature appears very similar to a gravity wave generated by a sudden increase, shortly
281 followed by a decrease, of a $n = 1$ heating profile (Nicholls et al. 1991).

282 By 1:35 simulation time, the low pressure anomaly is at approximately $x=225$ km (Fig. 7c).
283 The “widening” of the wave is largely due to the wave being advected slightly northward;
284 the x cross-section of the figure views the wave at an angle. (The updraft and downdraft
285 portions of the wave also move at slightly different speeds.) Taking into account the mean
286 tropospheric wind speed in direction of wave motion (-13.0 m s^{-1}) and the translation speed
287 of the domain (12.5 m s^{-1}), the modeled wave speed is an estimated 32 m s^{-1} . This is very
288 close to the estimated first observed feature speed of 32.5 m s^{-1} (Fig. 4a). Using the N of
289 the pre-storm environment in the simulation, 7.8×10^{-3} s^{-1} , and 12 km as the depth of the
290 troposphere, (1) predicts the speed of a $n = 1$ wave in this environment to be 29.8 m s^{-1} .
291 This is somewhat slower than both the modeled and observed speeds, but still very similar.

292 Also evident in Fig. 7c are four other features, at $x=120$ km, 145 km, 175 km, and 182
293 km, that appear very much like $n = 1$ gravity waves. To determine if these features are

294 also waves generated by surges in the $n = 1$ heating profile, a Hovmöller diagram of vertical
295 motion at 6 km was created (Fig. 8b). Six kilometers was selected as it is half the height
296 of the troposphere and vertical motion associated with a $n = 1$ wave should be strongest
297 there (Nicholls et al. 1991); this is observed in Fig. 7a. The mean microphysical heating
298 between 5.2 and 7.3 km, the closest three vertical levels above and below 6 km, was also
299 calculated (Fig. 8a). This was calculated along a 5 km y cross-section through the $n = 1$
300 wave pressure responses ($y=100.5$ to 105.5 km, shown in Fig. 7), and over the entire domain
301 in the x direction. It should be noted that the heating rates shown are averages over an area
302 and therefore of small magnitude. It is possible cells within that area have larger heating
303 fluctuations.

304 From Fig. 8, it can be seen that changes in the mean mid-level heating rate correspond
305 well with changing-amplitude signatures in the vertical motion field. For example, an in-
306 crease in heating between approximately 0:22 and 0:28 produces an area of subsidence that
307 propagates away from the source. The decrease in heating between 0:29 and 0:33 generates
308 an area of ascent that does the same. This process is repeated numerous times throughout
309 the simulation; as an illustration the five waves shown in Fig. 7c are marked on Fig. 8b
310 by thin black lines. The times of generation of each of these waves, as determined by first
311 visibility of the wave signature within the vertical motion field, are connected to the heating
312 rate at the same time by thin grey lines. Each upward motion response occurs in conjunction
313 with an decrease in the mid-level heating rate, although the decrease at 1:00 is small. The
314 variations in the heating rate appear regular or even quasi-periodic, similar to the periodic
315 convective development noted in Lane and Zhang (2011).

316 Figures 9a-e show in grey the mean microphysical heating profile, over the same cross-
317 section as Fig. 8a, at the time of generation of each of these fast-moving responses of upward
318 motion. Heating through almost the entire depth of the troposphere is evident in each,
319 typical of a $n = 1$ wave mode superimposed with one or more higher order modes associated
320 with low-level cooling. The profiles in black are from times shortly before wave generation;

321 each upward motion response is associated with a decrease in heating throughout the mid-
322 levels. This decrease corresponds to a decrease in the amplitude of the $n = 1$ mode of
323 heating.

324 The waves generating the vertical motion perturbations all propagate at approximately
325 the same speed, 32 m s^{-1} . This speed is very similar to the speed of all four pressure features
326 tracked across Oklahoma in Figs. 4a-d. Perturbations in pressure similar to those observed
327 in Fig. 3 are also evident in the simulated surface pressure (not shown). Therefore, it is a
328 reasonable assumption that these observed features were reflections at the surface of $n = 1$
329 gravity waves generated by variations in the convective heating profile.

330 Lane and Reeder (2001) found that the subsidence generated by a $n = 1$ wave due to an
331 increase in heating decreased the pre-storm convective available potential energy (CAPE)
332 in their study by approximately 240 J kg^{-1} , or 15% of the ambient environmental value.
333 Conversely, the wave produced due to a decrease in the first internal mode of heating should
334 lift, cool, and moisten the troposphere, increasing the CAPE. Figure 10 displays the CAPE
335 over the same horizontal cross-section as Fig. 8, with respect to time. As expected, the
336 variations in CAPE very closely match the gravity waves shown in Fig. 8b.

337 The first $n = 1$ wave front passage produced the largest variation in CAPE, a decrease
338 of 270 J kg^{-1} from 0:20 to 0:35 simulation time at $x=110 \text{ km}$. With each subsequent gravity
339 wave passage, the CAPE values vary approximately 200 J kg^{-1} , or about 6-8% with respect
340 to the initial sounding CAPE of 3294 J kg^{-1} . This is somewhat less than the Lane and
341 Reeder (2001) results, but their simulations used a more stable atmosphere, with an N of
342 0.0115 s^{-1} , as opposed to this study's 0.0078 s^{-1} ; higher potential temperature perturbations
343 are expected with increased stability. The convective inhibition (CIN) values (not shown) do
344 not vary significantly after passage of the first $n = 1$ wave; even the effects of that wave are
345 small, on the order of 3 J kg^{-1} . Because the largest magnitudes of vertical motion associated
346 with each $n = 1$ wave were located at approximately 6 km, and most of the CIN was located
347 in the 0-3 km layer, the lack of effect on CIN is not surprising. Most of the CAPE variations

348 were due to changes in the mid-level lapse rate around these peak vertical motions.

349 5. Pressure surge

350 a. Feature description

351 A surge of higher pressure ahead of the convective line can be seen in Fig. 6b, in the
352 same location where the convective line was beginning to bow. (Also evident are additional
353 $n = 1$ waves.) As discussed above, the observed pressure surge extended approximately 20
354 km ahead of the convective line. The surge in Fig. 6b extends approximately 5 km ahead of
355 the convective line, and will later extend as far as 12 km ahead of the convective line; but
356 both of these are a shorter distance than observed. The bowing portion of the simulated
357 convective line was much shorter than observed as well - approximately 25 km in length
358 instead of 100 km, meaning associated cooling would be of smaller size as well. However, the
359 simulated heating timeseries and associated $n = 1$ waves match very well with the observed
360 pressure perturbations, as discussed in the previous section. Thus, it is not unreasonable to
361 expect the processes generating the simulated surge to be similar to those generating the
362 observed surge.

363 Figure 11 displays a vertical cross-section through the surge immediately after its devel-
364 opment. A positive pressure perturbation (with respect to the initial state) ahead of the
365 convective line, between $x = 120$ and 125 km and reaching vertically to 2 km, is evident.
366 The general trend of pressure increasing toward the convective line continues from $x = 132$
367 km, however. The pre-storm pressure field has been significantly modified by the numerous
368 $n = 1$ wave features already propagating ahead of the convective line. Overall, the net
369 effect of these earlier waves was a decrease in surface pressure ahead of the system. Thus,
370 within Fig. 11 the general trend of increasing pressure is more relevant than absolute positive
371 or negative perturbations, and the pressure surge will be identified here as the increasing
372 pressure gradient between $x = 120$ to 132 km, from 0 to 2.5 km aloft.

373 A number of higher-frequency features are also noticeable in the cloud water and vertical

374 motion fields in Fig. 11, between $x = 125$ and 150 km and at approximately 2 km and 5 km
375 aloft. These features will be discussed in the Section 6. Unfortunately, because these high-
376 frequency features were in the same area as the pressure surge, the surge's exact structure
377 and evolution was difficult to determine.

378 To better examine the pressure surge another Hovmöller diagram, of surface pressure
379 along the same cross-section through the surge, was constructed (Fig. 12b). Because the
380 peak microphysical cooling occurred at 0.85 km, the mean microphysical heating near that
381 level (0.85 km) was examined and is displayed in Fig. 12a. Evident within Fig. 12b are a
382 number of compression waves, propagating at approximately 360 m s^{-1} , causing periodic
383 oscillations within the surface pressure and heating fields. As these oscillations are strongest
384 at the surface and do not appear above 4 km, propagate horizontally only, and do not have
385 any associated vertical velocity perturbations, the waves appear to be Lamb waves (Nicholls
386 and Pielke 2000; Fanelli and Bannon 2005). CM1 is a compressible model (Bryan and Fritsch
387 2002) so this type of behavior is expected and was formally evaluated by Smith and Bannon
388 (2008).

389 The five waves noted in Fig. 7c also appear in Fig. 12b as low pressure regions propagating
390 away from the convective line (marked by thin black lines). Not every $n = 1$ wave that is
391 visible in Fig. 8b is also evident at the surface. Due to variations in tropospheric wind shear
392 and stability, not all vertical levels of a gravity wave travel at the same speed (Bretherton
393 1966; Tulich et al. 2007). The first $n = 1$ wave has the strongest surface pressure response.
394 The subsidence associated with that wave lasts for the longest time period (Fig. 8b), resulting
395 in the low surface pressures.

396 Immediately prior to the appearance of the pressure surge, at approximately $1:43$ simula-
397 tion time, a strong increase in 0.85 -km cooling is evident in Fig. 12a. The cause and vertical
398 structure of the cooling will be discussed later, but its timing in relation to the pressure
399 surge is unmistakable. The surge cannot be a bore because there is not a sufficient density
400 discontinuity between the surface layer and the layer above (Fig. 5). The pressure surge

401 is also moving faster than the convective line and associated gravity current, which has a
402 speed of 7.6 m s^{-1} during the same period and is labeled in Fig. 12b. The pressure surge and
403 gravity current are clearly unique features in Fig. 12b and are separated by approximately
404 10 km at 2:25 simulation time. Thus, the evidence suggests that the pressure surge feature
405 is a gravity wave generated by increased cooling in the lower levels of the convective line.

406 From Fig. 11, the leading edge of the pressure surge can be delineated by the -0.25 hPa
407 contour. However, because of the oscillations in the low-level pressure field due to Lamb
408 waves, tracking the surge using this contour does not produce a constant speed. Evaluation
409 of Fig. 12b shows fluctuations in surface pressure with a period of approximately 1 min. Thus,
410 to minimize the error introduced by these fluctuations, two speeds of the surge-leading -0.25
411 hPa contour were calculated: one from 1:53 to 2:29 simulation time, and the other from 1:54
412 to 2:28, using two-minute intervals within these periods.

413 The two calculated speeds are displayed on Fig. 12b as grey and black dashed lines, and
414 they are very similar: 11.3 and 9.8 m s^{-1} , respectively. After calculating the mean speed and
415 removing the domain translation and mean wind in direction of surge motion, this yields a
416 feature speed of 11.0 m s^{-1} . Figure 9f shows an increase in low-level cooling immediately
417 prior to the surge extending to 4 km. Using (1) and the N calculated immediately in front
418 of the system at that time ($7.7 \times 10^{-3} \text{ s}^{-1}$), the predicted speed for a wave generated by
419 cooling extending to 4 km is 9.8 m s^{-1} . The two speeds agree reasonably well, particularly
420 considering the possible error added to the speed estimation by the Lamb and high-frequency
421 waves.

422 Haertel and Johnson (2000), hereafter HJ00, observed similar gravity wave behavior in
423 response to a moving source of cooling. In their Section 3b, a two-dimensional cooling source
424 extending to 4 km was prescribed to move at 10 m s^{-1} in a linear numerical model. The
425 cooling produced a gravity wave response moving at 13 m s^{-1} , or 3 m s^{-1} ahead of the cool
426 source. The response contained a positive pressure perturbation extending to approximately
427 3 km aloft, overtopped by a weak low pressure perturbation (see their Fig. 5b). Because

428 the cool source and wave speed were similar, the positive surface pressure perturbation was
429 amplified by over 20% compared to a similar simulation with a stationary cooling source.
430 As the speed of the pressure surge gravity wave and convective line are also similar in this
431 simulation, it is possible the pressure surge response is being enhanced by this effect.

432 In Lane and Reeder (2001), the heating profile generating a $n = 3$ wave extended to the
433 tropopause, and contained three antinodes consisting of low- and upper-level cooling and
434 mid-level warming. The resulting pressure perturbations combined to extend the depth of
435 the troposphere as well. In HJ00, the wave response was produced solely by low-level cooling,
436 and the pressure response also remained in the lower levels. The pressure responses in both
437 studies appeared very similar at lower levels, at least at time scales on the order of 2 h or
438 less; at longer time scales, the vertical propagation of the wave in HJ00 became evident. The
439 pressure surge gravity wave response appears to be produced solely by the low-level cooling.
440 Examination of the Scorer parameter for a wave speed of 11 m s^{-1} (not shown, but very
441 similar to Fig. 17) shows a trapping level around 2 km, which acts to trap the wave energy
442 associated with the surge in the lower levels. A pressure surge gravity wave produced in a
443 simulation with that trapping layer removed reached above 4 km.

444 The pressure surge observed in ASJ10 moved at a speed of 21.6 m s^{-1} , which is sig-
445 nificantly faster than seen in the simulation. However, a few factors must be considered.
446 The stability and mean wind of the environment through which the observed pressure surge
447 was propagating is not known. Only the ground-relative speed of the observed surge was
448 calculated. A mean environmental wind speed in the direction of the surge of 10.6 m s^{-1} , a not
449 implausible value, would mean the actual surge wave speed was 11.0 m s^{-1} , what was simulated
450 here. The observed surge could also have been generated by deeper low-level cooling than
451 was simulated; through (1) this would result in a faster wave. Nevertheless, this simulation
452 still provides a feasible mechanism that can generate the pressure surge ahead of the bowing
453 convective line seen so often by ASJ10.

454 *b. Low-level cooling source*

455 The cause of the sudden increase in the low-level cooling can be seen in the time-height
 456 cross-sections shown in Fig. 13. These are mean vertical profiles created at each output
 457 time by averaging over the horizontal width of the convective system and pressure surge
 458 in the x-direction, and 5 km about the pressure surge in the y-direction. (Averaging area
 459 shown in inset in Fig. 13a; this area travels with the convective line). The positive and
 460 negative u wind averages are calculated separately. Model gridpoints are separated into two
 461 groups, one containing points with rear-to-front flow; the other front-to-rear flow. The mean
 462 horizontal motion of each group is calculated and displayed separately, in Figs. 13b and c.
 463 This procedure allows examination of mean fields without the opposing fields canceling each
 464 other out. The magnitude of the intensity of the cold pool (C) is shown in Fig. 13d, and it is
 465 calculated using $C^2 = \int_0^h B dz$, where B is buoyancy, and h the height at which B becomes
 466 0. B is given by

$$467 \quad B = g \left(\frac{\theta - \bar{\theta}}{\bar{\theta}} + 0.61(q_v - \bar{q}_v) - q_t \right) \quad (3)$$

468 where g is gravitational acceleration, θ potential temperature, q_v water vapor mixing ratio,
 469 q_t total hydrometeor mixing ratio, and the bars designate environmental conditions. The
 470 maximum updraft speed and maximum low-level (below 4 km) downdraft speed are shown
 471 in Figs. 13e and f.

472 Initially, the storm-relative front-to-rear flow increases at 1:30 simulation time, at approx-
 473 imately 3.5 km aloft ([1] in Fig. 13c). Shortly thereafter, the convective updraft suddenly
 474 strengthens as well ([2] in Fig. 13e). The mid-level rear-to-front flow also shows a strong
 475 increase at this time, and it deepens up to 6 km and extends to the surface ([3] in Fig. 13b).
 476 Following this, at 1:45, a large increase in all three of the microphysical cooling fields ([4] in
 477 Fig. 13a) occurs immediately prior to the appearance of the pressure surge.

478 The sudden influx of dry air into the rear of the storm as surmised by Figs. 13b and 5,
 479 as well as the descent of the rear-to-front flow to the surface (Fig. 13b), led to these large
 480 increases in evaporation and melting. The vertical extent of the total cooling by evaporation,
 481 melting, and sublimation at this time is approximately 4 km (Fig. 13a). Cold pool intensity

482 significantly increases at this same time (Fig. 13d). Finally, at the time the surge can be
483 seen ahead of the convective line, 1:55, the convective downdraft suddenly strengthens even
484 further ([5] in Fig. 13f) and strong outflow appears at the surface ([6] in Fig. 13b).

485 It is unclear at this time what causes the first increase in mid-level front-to-rear flow at
486 1:30. However, after this point the sequence of events is what would be expected in new
487 bowing development (Weisman 1992; Weisman 1993; Weisman and Rotunno 2005; James et
488 al. 2006). The convective updraft strengthens, increasing heating aloft and strengthening the
489 mid-level pressure perturbation. This forces an increase in the rear-to-front flow, bringing
490 drier air into the system and aiding in evaporative and sublimation cooling. The increase in
491 microphysical cooling helps intensify the low-level downdrafts. All of these in combination
492 act to locally speed one portion of the convective line, creating a bow; the surface winds
493 increase as well. A gravity wave, shown at the surface by a surge in increasing pressure, is
494 produced by the strong increase in low-level cooling and travels ahead of the bowing segment
495 of the convective line.

496 Time-height cross-sections through a non-bowing section of the convective line at $Y =$
497 125 km, generated in the same manner as Fig. 13, are shown in Fig. 14. At 1:30, the storm-
498 relative front-to-rear inflow is approximately 2 m s^{-1} slower (Fig. 14c) than in the bowing
499 segment. Convective updraft speeds at this time are weaker (Fig. 14e), and reduced updraft
500 magnitudes are found in the lower levels (not shown). Significantly, after 1:40 the mean rear-
501 to-front flow at 4 km is almost half the magnitude of the rear-to-front flow in the bowing
502 segment (Fig. 14b), resulting in a reduced influx of dry air into the rear of the storm system.

503 As a result, the amount of microphysical cooling by melting and evaporation (Fig. 14a)
504 is only half the amount seen in the bowing segment (Fig. 13a). The cold pool itself is also
505 not as strong (Fig. 14d), resulting in a slower speed for this portion of the convective line
506 compared to the bowing portion. Without a strong increase in cooling, the resulting gravity
507 wave and surface pressure response is much weaker, and the pressure surge is not seen ahead
508 of this portion of the convective line (Fig. 6b). Low-level downdrafts are also not as strong

509 (Fig. 14f).

510 As the cooling (including sublimation) within the bowing segment generating the pressure
511 surge gravity wave extends to 4 km (Figs. 13a, 9f), the lifting on its leading edge should
512 also. Unfortunately, the signal of this vertical motion is masked by the high-frequency
513 features (Fig. 11). A low-pass Lanczos filter (Duchon 1979) with cutoff wavelength at 4
514 km, approximately the horizontal wavelength of the high-frequency features, was applied
515 horizontally to this cross-section. Unfortunately artificial features are introduced in the
516 vertical motion field by the filtering, particularly in the region near the convective line with
517 its highly varying vertical motions. However, there does appear to be a signal in the filtered
518 0.85-km vertical motion field associated with the pressure surge gravity wave of upward
519 (downward) motion on its leading (trailing) edge (not shown); HJ00 noted a similar low-
520 level vertical motion response to a moving cool source.

521 Examination of the 0.85-km filtered potential temperature and water vapor perturbation
522 fields reveals signals of cooling and moistening on the leading edge of the surge gravity wave,
523 and warming, but no drying, on the trailing edge, although these features were difficult to
524 distinguish from artificial features introduced by the filtering process (not shown). These
525 temperature perturbations are also similar to those observed by HJ00. The lack of drying
526 on the trailing edge was due to the additional moistening by high-frequency features noted
527 in the next section. In Figs. 15 and 10 an approximate 250 J kg^{-1} increase in the unfiltered
528 CAPE field is evident over the same area as the surge, from 3050 to 3300 J kg^{-1} . The CAPE
529 increase appears to be collocated with the warming without drying on the trailing edge of
530 the surge wave, although this is difficult to determine due to the artificial noise due to the
531 filtering. In any event, the pressure surge is associated with a non-negligible increase in
532 CAPE, and there is not an increase of similar magnitude along other, non-bowing portions
533 of the convective line without a pressure surge (Fig. 15).

534 Surprisingly, CIN was minimally affected by the pressure surge gravity wave (not shown).
535 The main signal shown in the CIN field was a result of the high-frequency features, discussed

536 is Section 6.

537 *c. Effect of pressure surge on updraft strength*

538 The increase in pre-system CAPE associated with the pressure surge gravity wave should
539 theoretically result in an increase in convective updraft strength. However, because convec-
540 tive updraft strength is also dependent on the tilt of that updraft, connecting variations in
541 the maximum updraft speed to variations in pre-system CAPE is not simple. As updraft tilt
542 increases, the convective updraft weakens due to downward motion incited by a stronger,
543 downward-directed pressure gradient (Parker 2010). The tilt of the updraft is typically de-
544 termined by the ratio of C to the low-level environmental storm-relative shear (Δu_{env}) where
545 a ratio of 1 is considered an upright updraft (Rotunno et al. 1988; Weisman and Rotunno
546 2004; Bryan et al. 2006). However, Weisman (1992) noted the importance of the rear inflow
547 jet in determining updraft tilt, instead using the following ratio:

$$548 \frac{C^2 - u_j^2}{\Delta u_{env}^2} = \frac{C_j^2}{\Delta u_{env}^2} \quad (4)$$

549 where u_j^2 is defined as $(u_H^2 - u_0^2)$, u_H is the storm-relative flow within the system at the
550 height of the cold pool, and u_0 the flow at the surface.

551 To better evaluate the effect of increases in CAPE on updraft speed, the tilt of the
552 updraft at the time must be determined. The ratio given in (4), $C_j^2/\Delta u_{env}^2$, was calculated
553 for both the bowing and non-bowing segments of the convective line. This ratio was selected
554 instead of $C/\Delta u_{env}$ because of obviously strong rear-to-front flow associated with this system
555 (Figs. 13b, 14b), and the importance of rear-to-front flow in bow echoes (Weisman 1993).
556 Timeseries of $C_j^2/\Delta u_{env}^2$ are displayed in Fig. 16a. u_H and u_0 were calculated at the point
557 of maximum C in the cross-section. Δu_{env} was the 0-2.5 km shear; in this case almost all
558 shear was confined below 2.5 km.

559 Due to the increased cooling and cold pool intensity after 1:40 in the bowing segment of
560 the convective line, $C_j^2/\Delta u_{env}^2$ increases significantly (Fig. 16a), even reaching values above 15
561 immediately after the pressure surge. Such a value suggests a very tilted updraft (Weisman

1992; Bryan et al. 2006). In addition to the intense cold pool, the rear-to-front flow within the bowing segment descends to the surface farther behind the convective line after 1:40 (not shown). A large negative value of u_j^2 results, also tilting the updraft farther rearward over the cold pool (Weisman 1992). The updraft in the non-bowing segment is more upright, with smaller $C_j^2/\Delta u_{env}^2$ values (Fig. 16a) due to a less intense cold pool (Fig. 14d) and slower surface-based rear-to-front flow (Fig. 14b). Based on this information alone, the convective updraft within the bowing segment would be expected to be weaker than its non-bowing counterpart during this time period.

However, the bowing segment updraft is stronger than the updraft in the non-bowing segment, particularly from 1:55 to 2:00, and 2:05 to 2:10 (Fig. 16b), during and shortly after the generation of the pressure surge gravity wave. The increased CAPE generated by the pressure surge and high-frequency gravity waves aids in producing these stronger updraft magnitudes, despite the increased tilting of the updraft. The magnitude of the CAPE ahead of the non-bowing segment is not as large (Fig. 15), and the associated updraft is not as strong (Fig. 14e) during the same time period.

6. High-frequency gravity waves

In Fig. 11b, a series of updraft-downdraft couplets are located between approximately 2 and 2.5 km aloft, and $x=125$ and 150 km. Couplets of this nature are noted at this height as early as 30 minutes into the simulation. Within the updraft portion of these couplets condensation regularly occurs and clouds form (Fig. 11a). These features appear remarkably similar to those observed in Fovell et al. (2006) in association with high-frequency gravity waves generated by multicellularity in the convective line. While the speed of these features varied, an average speed at the time of the pressure surge is estimated at -3.6 m s^{-1} ; this is an actual phase speed of 6.5 m s^{-1} once the mean wind at that level (2.4 m s^{-1}) and the domain translation (12.5 m s^{-1}) is accounted for.

Unlike the low-frequency gravity waves discussed above, these higher-frequency waves require a trapping level other than the tropopause so their energy does not propagate verti-

589 cally immediately. In Fovell et al. (2006), the trapping level was provided by the curvature of
 590 the wind profile due to outflow aloft at anvil level. However, the vertical motions associated
 591 with the high-frequency gravity waves in that study extended to 7 km. Here, the couplets
 592 are trapped in a layer around 2 km.

593 An examination of the environmental stability explains this (Fig. 17). The Scorer pa-
 594 rameter was calculated as in Fovell et al. (2006), as

$$595 \quad l^2 = \frac{N_m^2}{(U - c)^2} - \frac{\partial^2 U / \partial z^2}{(U - c)} \quad (5)$$

596 where N_m^2 is the Brunt-Väisälä frequency, calculated separately for saturated and subsatu-
 597 rated air as discussed in Section 1, U ground-relative wind speed, z height, and c the average
 598 high-frequency ground-relative wave speed, 6.5 m s^{-1} . A thin stable layer is evident between
 599 approximately 2 and 2.5 km. Both above and below this layer are regions where the Scorer
 600 parameter is negative, which act to reflect the wave energy. Thus, the updraft couplets and
 601 associated clouds remain in the 2 to 2.5 km layer. A similar trapping level is also evident just
 602 below 6 km (Fig. 17), with updraft-downdraft couplets and cloud development immediately
 603 below (Fig. 11). A simulation was run with the trapping levels around 2 km removed, and
 604 no high-frequency wave features were found in that region. High-frequency waves were still
 605 found just below 6 km, as that trapping level was unmodified.

606 It was also noted by Fovell et al. (2006) that these high-frequency gravity waves can
 607 have an effect on the pre-storm environment, particularly when condensation occurs within
 608 an associated updraft and forms a cloud. The latent heat released would act to modify the
 609 parcel's stability; if ingested into the storm the extra warmth and moisture would intensify
 610 the system. However, if the cloud became large enough to produce rain, it could create
 611 its own cold pool, which would instead have a negative effect when ingested. In this case,
 612 none of the clouds produced rain or had individual cold pools, so the feedback to the system
 613 should be positive. The effect of the latent heat release on the stability of the 2 to 2.5 km
 614 layer can be seen within Fig. 17 between $x=125$ and 130 km: the latent heat release from
 615 the formation of multiple clouds, and the turbulent mixing associated with this, mixed out

616 the stable layer and decreased the overall stability.

617 Increases in CAPE due to these small clouds can be seen in Fig. 15. The magnitude of
618 these increases are largest within the pressure surge: small cells containing CAPE values
619 larger than 3500 J kg^{-1} can be seen immediately ahead of the convective line within the
620 pressure surge in Fig. 15. This effect can also be seen in Fig. 10. One specific cloud (and
621 associated increase in CAPE) is tracked in Fig. 10 by a thin dashed black line. The formation
622 of the cloud was associated with increased CAPE (approximately 200 J kg^{-1}) and decreased
623 CIN (approximately 2 J kg^{-1} , not shown). However, within the CAPE field (Fig. 10) the
624 variations associated with these high-frequency features appear largest in magnitude, by
625 approximately 50 J kg^{-1} , after passage of the pressure surge gravity wave.

626 As in Fovell et al. (2006), the low-frequency wave “prepares” the environment for later
627 high-frequency features by gently lifting of its leading edge the lower levels of the troposphere.
628 This allows the later high-frequency features to generate much stronger variations in CAPE
629 by forming clouds in this newly-moistened layer. Once a cloud is formed due to lifting from
630 the high-frequency wave, it does not travel with the wave, but instead is advected by the
631 mean flow at that level. Within Fig. 10, the thin dashed line is used to track the speed of one
632 of the clouds at -11.4 m s^{-1} . Accounting for the 12.5 m s^{-1} domain translation, the cloud
633 moves at the speed of the mean wind at that level. It is advected toward the system as in
634 Fovell et al. (2006). Small clouds forming immediately ahead of, and then being overtaken
635 by, the convective line were detected by the KTLX WSR-88D from 0516 though 0635 UTC
636 (not shown).

637 7. Conclusions

638 A number of surface pressure features observed by Adams-Selin and Johnson (2010) in
639 conjunction with the 13 March 2003 bow echo over Oklahoma are further evaluated, us-
640 ing both additional examination of the observations and a high-resolution numerical model
641 simulation. The observed surface pressure features include one approximately 2 hPa tempo-
642 rary decrease in pressure that propagates quickly away from the convective line at 32.5 m

643 s^{-1} , followed by a subsequent rise, dip, and rise in pressure. These pressure perturbations
644 propagate away at approximately the same speed. Also observed is a surge of increasing
645 pressure ahead of the convective line. Pressure surges of this nature were observed in 35 of
646 39 bow echoes examined by Adams-Selin and Johnson (2010). The surges generally occurred
647 immediately prior to or at the same time as the bow echo developed.

648 A numerical simulation is performed to understand the processes generating these fea-
649 tures. In the simulation, numerous gravity waves are generated by the evolving heating
650 profile. Fluctuations in the amplitude of deep convective heating generate $n = 1$ gravity
651 wave responses that travel quickly away from the convective line, as theorized by Nicholls
652 et al. (1991). An increase in the heating results in a wave with subsidence throughout the
653 tropospheric column and corresponding warming and drying with a low surface pressure
654 perturbation; a decrease in that profile results in a wave with ascent throughout the column,
655 and subsequent cooling and moistening with a high surface pressure perturbation.

656 Not only do the modeled $n = 1$ waves propagate at nearly the same speed as the observed
657 fast-moving low pressure feature (32 m s^{-1} and 32.5 m s^{-1} , respectively), the vertical struc-
658 ture of the modeled feature matches theoretical studies (Nicholls et al. 1991) exactly. Thus,
659 it is concluded that the observed fast-moving pressure features are indeed $n = 1$ gravity
660 waves. Wave generation is also very frequent and associated with fluctuations in the $n = 1$
661 heating profile. Eighteen $n = 1$ waves are produced just in this 2.6-h simulation, and surface
662 reflections of four $n = 1$ waves are noted in the observations. Within the simulation, each
663 $n = 1$ wave modifies the pre-storm CAPE profile by between 6 to 8% of the initial CAPE
664 value.

665 A surge of increasing pressure occurs ahead of the bowing segment of the convective
666 line as bowing develops. This simulated pressure feature propagates at a speed of approx-
667 imately 11.0 m s^{-1} , in good agreement with a gravity wave postulated to be excited by
668 strong low-level cooling extending to 4 km with a speed of 9.8 m s^{-1} . Shortly prior to surge
669 development, the system's front-to-rear inflow and convective updraft increases within this

670 segment, strengthening the mid-level pressure perturbation, and resulting in an increase in
671 rear-to-front flow. This increases low-level microphysical cooling and convective downdrafts
672 up to 4 km by introducing additional dry air; the cooling generates the gravity wave. An
673 approximate 250 J kg^{-1} increase in CAPE, or 8% of the initial sounding, is noted in con-
674 junction with the combination of the pressure surge and other higher-frequency features,
675 suggesting lifting and moistening is occurring at lower levels. This higher CAPE partially
676 explains the increasing strength of the convective updraft in the bowing segment at time of
677 bowing, despite increased updraft tilt due to a strengthening cold pool and surface-based
678 rear-to-front flow.

679 The larger magnitudes of rear-to-front flow and low-level microphysical cooling rates,
680 generation of the gravity wave and pressure surge, and resulting higher pre-system CAPE
681 are all confined to the bowing segment of the convective line and the area immediately in
682 advance of it. A non-bowing convective segment was examined, which exhibits rear-to-front
683 flow and low-level microphysical cooling rates of half the magnitude of those in the bowing
684 segment. The convective updraft strength at time of bowing was also weaker, despite a less
685 pronounced updraft tilt.

686 The appearance of the pressure surge can be explained in the context of Haertel and John-
687 son (2000) wherein the linear response to a moving low-level cool source was investigated.
688 In that study it was found that when the gravity wave speed associated with the vertical
689 scale of the cooling approximately matched the speed of the cool source, an amplification of
690 the surface pressure response occurred. The modeling results here are analogous.

691 Finally, a number of high-frequency features, updraft-downdraft couplets that produced
692 small clouds, are trapped in the 2 to 2.5 km stable layer in advance of the system. These
693 features are similar to those modeled by Fovell et al. (2006), although in this case they are
694 trapped by a much lower unstable layer as opposed to the curvature of the wind profile due
695 to the outflowing anvil aloft. The latent heat release associated with the clouds that form
696 within the updraft portion of each wave modifies the pre-storm stable layer by decreasing its

697 stability and the environmental CIN, and increasing the CAPE. However, these effects are
698 more noticeable after passage of the pressure surge. The more gentle lifting generated by that
699 low-frequency wave moderately moistens the lower troposphere, allowing larger destabilizing
700 effects to be generated by the high frequency features. The results support the mechanisms
701 described by Fovell et al. (2006).

702 The results herein have multiple implications for current convective modeling. As has
703 already been noted in other studies (Lane and Reeder 2001), these types of gravity waves
704 have a significant effect on the pre-storm environment. However, in this study waves are
705 continually generated by both strengthening and weakening of the convective heating profile.
706 Wave fronts generated in response to a weakening of the amplitude of the $n = 1$ heating
707 profile had not been previously observed except in theory (Nicholls et al. 1991). Each
708 passage of just one of these waves significantly modifies the pre-storm environment, making
709 characterization of the pre-storm environment much more difficult than previously supposed.

710 The lifting and subsequent destabilization created by the pressure surge gravity wave, and
711 associated increase in updraft strength, would positively feed back to the system, helping
712 it further intensify as the bowing process occurs. This indicates that the gravity waves
713 generated by a system can have a feedback effect of short time scales. An interesting point is
714 that this simulated bow echo had not yet produced large amounts of stratiform precipitation.
715 Typically higher vertical wave modes are associated with melting and evaporation in the
716 stratiform region; this case shows that such a profile can be created within the convective
717 region alone.

718 The importance of low-level cooling in generation of new bowing development is under-
719 scored by this study, particularly as Adams-Selin and Johnson (2010) observed this pressure
720 surge feature in conjunction with many developing bow echoes. As rear-to-front flow and
721 convective downdrafts are key in producing the low-level cooling seen here, the characteris-
722 tics of the source of these flows - the ambient environmental conditions - are of consequence.
723 Furthermore, these simulated cooling rates highly depend on the chosen microphysical pa-

724 rameterization. This highlights the significance of correctly parameterizing microphysical
725 processes when simulating bow echo development, which is still an area of active work.

726 **8. Acknowledgments**

727 This research was supported by National Science Foundation Grant ATM-0500061. Ok-
728 lahoma Mesonet data were provided through the courtesy of the Oklahoma Mesonet, a
729 cooperative venture between Oklahoma State University and the University of Oklahoma
730 and supported by the taxpayers of Oklahoma. The WSI NOWrad data were provided by
731 the Mesoscale and Microscale Meteorology Division of the University Corporation for Atmo-
732 spheric Research (UCAR) through David Ahijevych. Computing resources were provided by
733 the Navy Department of Defense Supercomputing Resource Center (Navy DSRC) and the
734 Army Research Laboratory Department of Defense Supercomputing Resource Center (ARL
735 DSRC), which are sponsored by the DoD High Performance Computing Modernization Pro-
736 gram. The authors would like to thank Susan van den Heever and Russ Schumacher of
737 CSU, and Morrison Weisman of UCAR, for many discussions regarding this work. We also
738 thank George Bryan for assistance in using the CM1 model. Patrick Haertel aided with data
739 interpretation of the Oklahoma Mesonet data. The comments of three anonymous reviewers
740 were greatly appreciated.

REFERENCES

- 741 Adams-Selin, R. D., and R. H. Johnson, 2010: Mesoscale surface pressure and temperature
742 features associated with bow echoes. *Mon. Wea. Rev.*, **138**, 212–227.
- 743 Bretherton, C. S., and P. K. Smolarkiewicz, 1989: Gravity waves, compensating subsidence
744 and detrainment around cumulus clouds. *J. Atmos. Sci.*, **46**, 740–759.
- 745 Bretherton, F. P., 1966: The propagation of groups of internal gravity waves in a shear flow.
746 *Quart. J. Roy. Meteorol. Soc.*, **92**, 466–480.
- 747 Bryan, and J. M. Fritsch, 2002: A benchmark simulation for moist nonhydrostatic numerical
748 models. *Mon. Wea. Rev.*, **130**, 2917–2928.
- 749 —, and R. Rotunno, 2009: The maximum intensity of tropical cyclones in axisymmetric
750 numerical model simulations. *Mon. Wea. Rev.*, **137**, 1770–1789.
- 751 —, and M. D. Parker, 2010: Observations of a squall line and its near environment using
752 high-frequency rawinsonde launches during VORTEX2. *Mon. Wea. Rev.*, **138**, 4076–
753 4097.
- 754 —, J. C. Knievel, and M. D. Parker, 2006: A multimodel assessment of RKW Theory’s
755 relevance to squall-line characteristics. *Mon. Wea. Rev.*, **134**, 2772–2792.
- 756 Duchon, C. E., 1979: Lanczos filtering in one and two dimensions. *J. App. Meteor.*, **18**,
757 1016–1022.
- 758 Fanelli, P. F., and P. R. Bannon, 2005: Nonlinear atmospheric adjustment to thermal forcing.
759 *J. Atmos. Sci.*, **62**, 4253–4272.

- 760 Fovell, R. G., 2002: Upstream influence of numerically simulated squall-line storms. *Quart.*
761 *J. Roy. Meteorol. Soc.*, **128**, 893–912.
- 762 —, G. L. Mullendore, and S. H. Kim, 2006: Discrete propagation in numerically simulated
763 nocturnal squall lines. *Mon. Wea. Rev.*, **134**, 3735–3752.
- 764 Gallus, W. A., Jr., and R. H. Johnson, 1991: Heat and moisture budgets of an intense
765 midlatitude squall line. *J. Atmos. Sci.*, **48**, 122–146.
- 766 Haertel, P. T., and R. H. Johnson, 2000: The linear dynamics of squall line mesohighs and
767 wake lows. *J. Atmos. Sci.*, **57**, 93–107.
- 768 —, R. H. Johnson, and S. N. Tulich, 2001: Some simple simulations of thunderstorm
769 outflows. *J. Atmos. Sci.*, **58**, 504–516.
- 770 Houze, R. A., Jr., 1982: Cloud clusters and large-scale vertical motions in the tropics. *J.*
771 *Meteor. Soc. Japan*, **60**, 396–410.
- 772 James, R. P., J. M. Fritsch, and P. M. Markowski, 2006: Bow echo sensitivity to ambient
773 moisture and cold pool strength. *Mon. Wea. Rev.*, **134**, 950–963.
- 774 Johnson, R. H., and G. S. Young, 1983: Heat and moisture budgets of tropical mesoscale
775 anvil clouds. *J. Atmos. Sci.*, **40**, 2138–2147.
- 776 —, and B. E. Mapes, 2001: Mesoscale processes and severe convective weather. C. A.
777 Doswell III, Ed., AMS Monograph, *Severe Convective Weather*, **28**, 71–122.
- 778 Klemp, J. B., 1994: On the dynamics of gravity currents in a channel. *J. Fluid Mech.*, **269**,
779 169–198.

- 780 Knupp, K., 2006: Observational analysis of a gust front to bore to solitary wave transition
781 within an evolving nocturnal boundary layer. *J. Atmos. Sci.*, **63**, 2016–2035.
- 782 Lane, T. P., and M. J. Reeder, 2001: Convectively generated gravity waves and their effect
783 on the cloud environment. *J. Atmos. Sci.*, **58**, 2427–2440.
- 784 —, and M. W. Moncrieff, 2008: Stratospheric gravity waves generated by multiscale tropical
785 convection. *J. Atmos. Sci.*, **65**, 2598–2614.
- 786 —, and F. Zhang, 2011: Coupling between gravity waves and tropical convection at
787 mesoscales. *J. Atmos. Sci.*, **68**, 2585–2598.
- 788 Liu, C., M. W. Moncrieff, 2004: Effects of convectively generated gravity waves and rotation
789 on the organization of convection. *J. Atmos. Sci.*, **61**, 2218–2227.
- 790 Mapes, G. E., 1993: Gregarious tropical convection. *J. Atmos. Sci.*, **50**, 2026–2037.
- 791 McAnelly, R. I., J. E. Nachamkin, W. R. Cotton, and M. E. Nicholls, 1997: Upscale evolution
792 of MCSs: Doppler radar analysis and analytical investigation. *Mon. Wea. Rev.*, **125**,
793 1083–1110.
- 794 Nicholls, M. E., 1987: A comparison of the results of a two-dimensional numerical simulation
795 of a tropical squall line with observations. *Mon. Wea. Rev.*, **115**, 3055–3077.
- 796 —, R. A. Pielke, 2000: Thermally induced compression waves and gravity waves generated
797 by convective storms. *J. Atmos. Sci.*, **57**, 3251–3271.
- 798 —, —, and W. R. Cotton, 1991: Thermally forced gravity waves in an atmosphere at rest.
799 *J. Atmos. Sci.*, **48**, 1869–1884.

- 800 Pandya, R. E., and D. R. Durran, 1996: The influence of convectively generated thermal
801 forcing on the mesoscale circulation around squall lines. *J. Atmos. Sci.*, **53**, 2924–2951.
- 802 —, D. R. Durran, and M. L. Weisman, 2000: The influence of convective thermal forcing
803 on the three-dimensional circulation around squall lines. *J. Atmos. Sci.*, **57**, 29–45.
- 804 Parker, M. D., 2008: Response of simulated squall lines to low-level cooling. *J. Atmos. Sci.*,
805 **65**, 1323–1341.
- 806 —, 2010: Relationship between system slope and updraft intensity in squall lines. *Mon.*
807 *Wea. Rev.*, **138**, 3572–3578.
- 808 Rotunno, R., J. B. Klemp, and M. L. Weisman, 1988: A theory for strong, long-lived squall
809 lines. *J. Atmos. Sci.*, **45**, 463–485.
- 810 Schmidt, J. M., and W. R. Cotton, 1990: Interactions between upper and lower tropospheric
811 gravity waves on squall line structure and maintenance. *J. Atmos. Sci.*, **47**, 1205–1222.
- 812 Schumacher, R. S., 2009: Mechanisms for quasi-stationary behavior in simulated heavy-rain
813 producing convective systems. *J. Atmos. Sci.*, **66**, 1543–1568.
- 814 Smith, J. W., and P. R. Bannon, 2008: A comparison of compressible and anelastic models
815 of deep dry convection. *Mon. Wea. Rev.*, **136**, 4555–4571.
- 816 Stensrud, D. J., M. C. Coniglio, R. P. Davies-Jones, and J. S. Evans, 2005: Comments on
817 “A theory for strong long-lived squall lines’ revisited.” *J. Atmos. Sci.*, **62**, 2989–2996.
- 818 Thompson, G., P. R. Field, R. M. Rasmussen, and W. D. Hall, 2008: Explicit forecasts of
819 winter precipitation using an improved bulk microphysics scheme. Part II: Implementa-
820 tion of a new snow parameterization. *Mon. Wea. Rev.*, **136**, 5095–5115.

- 821 Tulich, S. N., D. A. Randall, B. E. Mapes, 2007: Vertical-mode and cloud decomposition
822 of large-scale convectively coupled gravity waves in a two-dimensional cloud-resolving
823 model. *J. Atmos. Sci.*, **64**, 1210–1229.
- 824 Wakimoto, R. M., 1982: Life cycle of thunderstorm gust fronts as viewed with Doppler radar
825 and rawinsonde data.
- 826 Weisman, M. L., 1992: The role of convectively generated rear-inflow jets in the evolution
827 of long-lived mesoconvective systems. *J. Atmos. Sci.*, **49**, 1826–1847.
- 828 —, 1993: The genesis of severe long-lived bow echoes. *J. Atmos. Sci.*, **50**, 645–670.
- 829 —, and R. Rotunno, 2004: “A theory for strong long-lived squall lines” revisited. *J. Atmos.*
830 *Sci.*, **61**, 361–382.
- 831 —, and —, 2005: Reply. *J. Atmos. Sci.*, **62**, 2997–3002.
- 832 —, W. C. Skamarock, and J. B. Klemp, 1997: The resolution dependence of explicitly
833 modeled convective systems. *Mon. Wea. Rev.*, **125**, 527–548.

FIGURE CAPTIONS

835 Figure 1. (a-d): Signal of a $2.0 \text{ J kg}^{-1} \text{ s}^{-1}$ convective ($n = 1$) heating pulse underneath a rigid lid
836 at 10 km. The time is 4 hours after start of heating; the heating was turned on initially
837 and then turned off after 2 h. (a) Horizontal velocity (0.3 m s^{-1} , negative dashed);
838 (b) vertical velocity (3 cm s^{-1} , negative dashed); (c) perturbation pressure (12 Pa ;
839 negative dashed); (d) perturbation buoyancy (0.005 m s^{-2}). The heating source is at
840 $x=0 \text{ km}$. (e-h): As in (a-d), but the heating source is the combined $n = 1$ and $n = 2$
841 heating modes, of magnitude $1.0 \text{ J kg}^{-1} \text{ s}^{-1}$, and is not turned off. The time is 2 hours
after start of heating. Adapted from Figs. 10 and 5 of Nicholls et al. (1991).

842 Figure 2. WSI NOWrad base reflectivity from 0230 (a), 0345 (b), 0515 (c), 0545 (d), 0615 (e),
843 and 0830 (f) UTC 13 March 2003. High-pass filtered potential temperature (purple,
844 1°C), surface wind (black, barbs) and adjusted pressure (black, 0.5 hPa). High and
845 low pressure maxima are denoted by “H” and “L” respectively. The star is the KTLX
846 radar, and the black dots in (a) are Oklahoma mesonet stations VANO and HUGO.
847 (From ASJ10.)

848 Figure 3. Timeseries display of high-pass filtered data from stations VANO (a) and HUGO (b)
849 from the Oklahoma Mesonet (locations shown in Fig. 2a). Time increases to the left
850 from 0300 to 0800 UTC 13 March 2003. Upper graphs in each figure show potential
851 temperature (K, dashed, upper right scale) and adjusted pressure (hPa, solid line,
852 upper left scale). Lower graphs show sustained winds (knots, barbs), sustained wind
853 speed (m s^{-1} , solid line, lower left scale), unfiltered wind gusts (m s^{-1} , G, lower left
854 scale), and unfiltered precipitation rate (mm (5 min)^{-1} , dashed line, lower right scale).
855 [a] - [f] refer to indications of passing gravity waves or gravity current at each station
856 and are referenced in the text.

854 Figure 4. Isochrones (grey, contoured every 30 min) for the features noted in Fig. 3 at arrows [a],
858 [b], [c], [d], and [e], corresponding to figure (a), (b), (c), (d), and (e), here, respectively.
859 Only stations where each feature was observed are included (some stations are omitted
860 for display clarity). Times are displayed in decimal format (e.g., 4.33 is 0420 UTC 13
861 March 2003).

862 Figure 5. 0000 UTC 13 March 2003 KOUN sounding, with temperature (black, °C) and dewpoint
863 (gray, °C).

864 Figure 6. Simulated reflectivity (filled contours, dBZ) and pressure perturbation (black, 0.25
865 hPa, negative dashed) at the lowest staggered model level, 50 m, for (a) 0:50 and
866 (b) 1:50 simulation time. Black arrows point to the $n=1$ waves and pressure surge
867 discussed in Sections 4 and 5, respectively.

868 Figure 7. Vertical x cross-sections from 0-12 km, through the low pressure anomaly, averaged 5
869 km about the x cross-section ($y=100.5$ to 105.5 km). (a) Vertical wind speed (color,
870 m s^{-1}) and pressure perturbation (black, 0.2 hPa, negative dashed) at 0:50 simulation
871 time. Upward and downward motion indicated by arrows; high and low pressure
872 perturbations by “H” and “L”. (b) Potential temperature perturbation (color, K) and
873 u wind perturbation (black, 1 m s^{-1} , negative dashed) at 0:50 simulation time. Inflow
874 and outflow indicated by arrows. (c) As in (a), but for 1:35 simulation time. The wave
875 in (a), and the rightmost wave in (c), are the same feature.

876 Figure 8. (a) Mean microphysical heating (K (1 min)^{-1}) between 5.2 and 7.3 km aloft, $y=100.5$
877 to 105.5 km as in Fig. 7, and across the entire domain in the x direction, from 0:00 to
878 3:00 simulation time. (b) Time evolution of horizontal distribution of vertical motion
879 (m s^{-1}) at 6 km aloft, averaged 5 km about the x cross-section. Signature of the five
880 gravity waves discussed in Section 4, and shown in Fig. 7c, are denoted by black lines.
881 Grey lines connect the time of initial generation of these waves to the heating rate at
882 the same time.

Figure 9. Mean microphysical heating profiles (1×10^{-2} K (1 min) $^{-1}$) between $y=100.5$ to 105.5
884 km (5 km about pressure surge) and across the entire domain in the x direction. Grey
885 lines in (a-e) show the heating profile at the time of wave generation (waves shown
886 in Fig. 8), black lines are the profiles from shortly before generation. (f) shows the
887 heating profiles shortly before (black) and at the time of (grey) development of the
888 pressure surge gravity wave. Times of each profile are noted in each subfigure.

Figure 10. Time evolution of horizontal distribution of CAPE (color, 45 J kg^{-1}), averaged 5 km
890 about the x cross-section as in Fig. 8b. Five thin black lines track the five gravity
891 waves discussed in Section 4 and shown in Fig. 7. Thick dashed grey and black lines
892 denote the pressure surge discussed in Section 5. Thin dashed black line tracks a cloud
893 generated by a high-frequency gravity wave, discussed in Section 6.

Figure 11. Vertical x cross-sections from $0-12$ km, through the low pressure anomaly, averaged
895 5 km about the x cross-section. (a) Vertical wind speed (color, m s^{-1}) and pressure
896 perturbation (black, 0.2 hPa, negative dashed) at $0:50$ simulation time. Upward and
897 downward motion indicated by arrows; high and low pressure perturbations by “H” and
898 “L”. (b) Potential temperature perturbation (color, K) and u wind perturbation (black,
899 1 m s^{-1} , negative dashed) at $0:50$ simulation time. Inflow and outflow indicated by
900 arrows. (c) As in (a), but for $1:35$ simulation time. The wave in (a), and the rightmost
901 wave in (c), are the same feature.

Figure 12. (a) Mean microphysical heating (K (1 min) $^{-1}$) between 0.65 and 1.05 km aloft, $y=100.5$
903 to 105.5 km (5 km about pressure surge), and across the entire domain in the x-
904 direction. (b) Time evolution of surface pressure perturbation (hPa) averaged 5 km
905 about the x cross-section. Thin black lines are as in Fig. 8b. The thick dashed black
906 and grey lines show the progression of the pressure surge feature.

Figure 13. Time-height series of mean vertical profiles, created by averaging over the horizontal
908 width of the system and pressure surge in the x-direction, and 5 km about the pressure

909
910
911
912
913
914
915
916
917

surge and bow echo in the y-direction. Area averaged over shown in inset in (a); area moves with convective line. The positive and negative u wind averages were calculated separately. The thin black vertical line in each is the time of the start of the pressure surge. (a) Microphysical cooling rates due to evaporation (filled contours, $\text{K} (5 \text{ min})^{-1}$), melting (red, $0.01 \text{ K} (5 \text{ min})^{-1}$), and sublimation (purple, $0.02 \text{ K} (5 \text{ min})^{-1}$). (b) Storm-relative front-to-rear u wind (1.5 m s^{-1}). (c) Storm-relative rear-to-front u wind (1 m s^{-1}). (d) Maximum cold pool intensity (C , m s^{-1}). (e) Maximum upward vertical motion (1 m s^{-1}). (f) Maximum downward vertical motion (1.0 m s^{-1}). Labels [1] through [6] detail the bowing process and are discussed in the text.

Figure 14. As in Fig. 13, but for a non-bowing segment of the convective line, shown in inset in (a).

919

921

Figure 15. CAPE (color, J kg^{-1}) and pressure perturbation (black, 0.5 hPa, negative dashed) at 1:55 simulation time.

Figure 16. (a) $C_j^2/\Delta u_{env}^2$ for cross-sections through the pressure surge and bowing convective line (solid) and through $y=125 \text{ km}$, a non-bowing segment of the convective line (dashed). (b) Difference between maximum convective updraft in the bowing and non-bowing segments of the convective line. Thin black vertical line in both indicates time pressure surge first appeared ahead of the convective line.

923
924
925
926

Figure 17. Vertical 0-12 km cross-section at 1:55 simulation time, averaged 5 km about x-axis, of the Scorer parameter (color, $1 \times 10^{-6} \text{ m}^{-2}$) for a wave speed of 6.5 m s^{-1} . Black box delineates the same area as in Fig. 11.

928
929

FIGURES

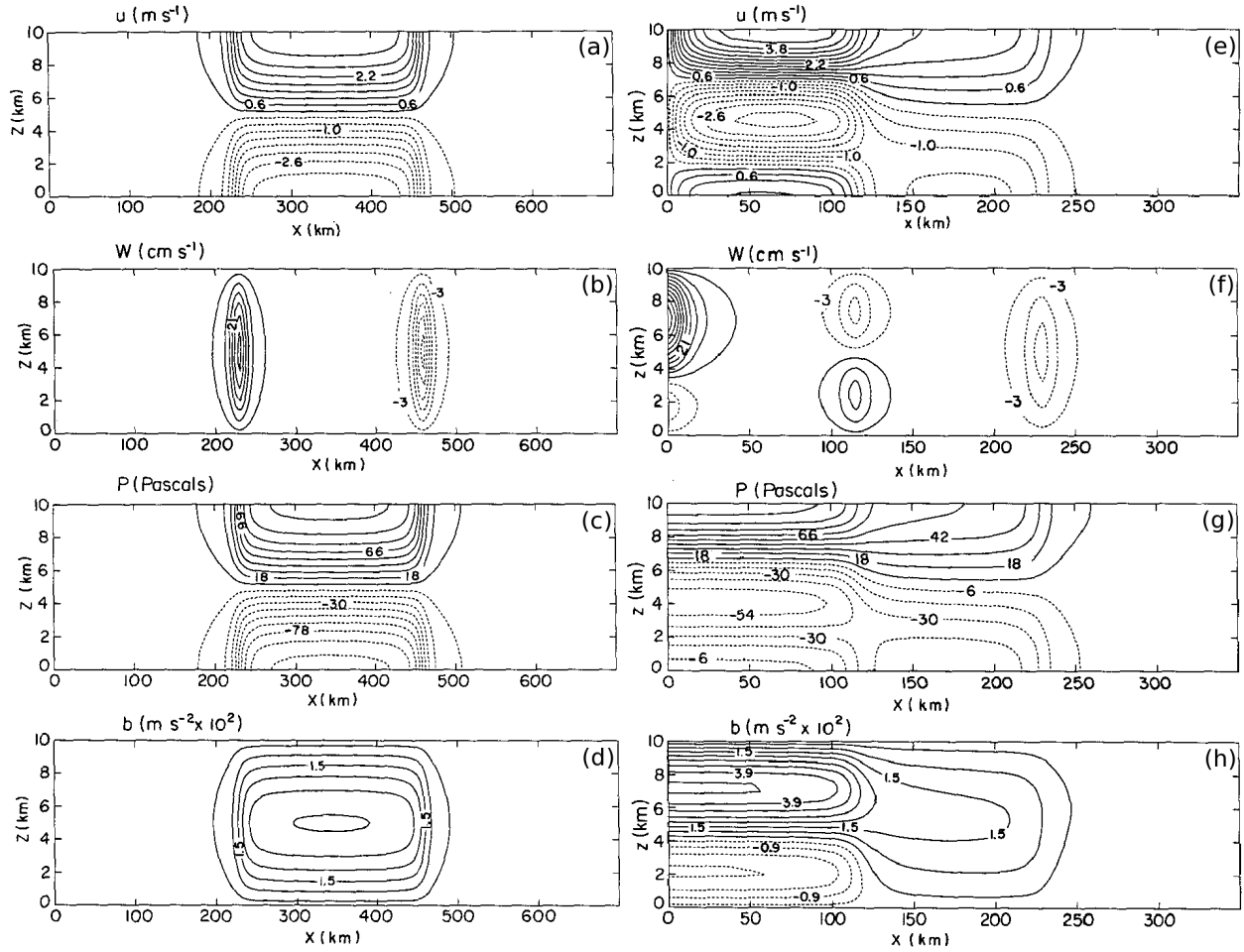


Figure 1: (a-d): Signal of a $2.0 \text{ J kg}^{-1} \text{ s}^{-1}$ convective ($n = 1$) heating pulse underneath a rigid lid at 10 km. The time is 4 hours after start of heating; the heating was turned on initially and then turned off after 2 h. (a) Horizontal velocity (0.3 m s^{-1} , negative dashed); (b) vertical velocity (3 cm s^{-1} , negative dashed); (c) perturbation pressure (12 Pa; negative dashed); (d) perturbation buoyancy (0.005 m s^{-2}). The heating source is at $x=0 \text{ km}$. (e-h): As in (a-d), but the heating source is the combined $n = 1$ and $n = 2$ heating modes, of magnitude $1.0 \text{ J kg}^{-1} \text{ s}^{-1}$, and is not turned off. The time is 2 hours after start of heating. Adapted from Figs. 10 and 5 of Nicholls et al. (1991).

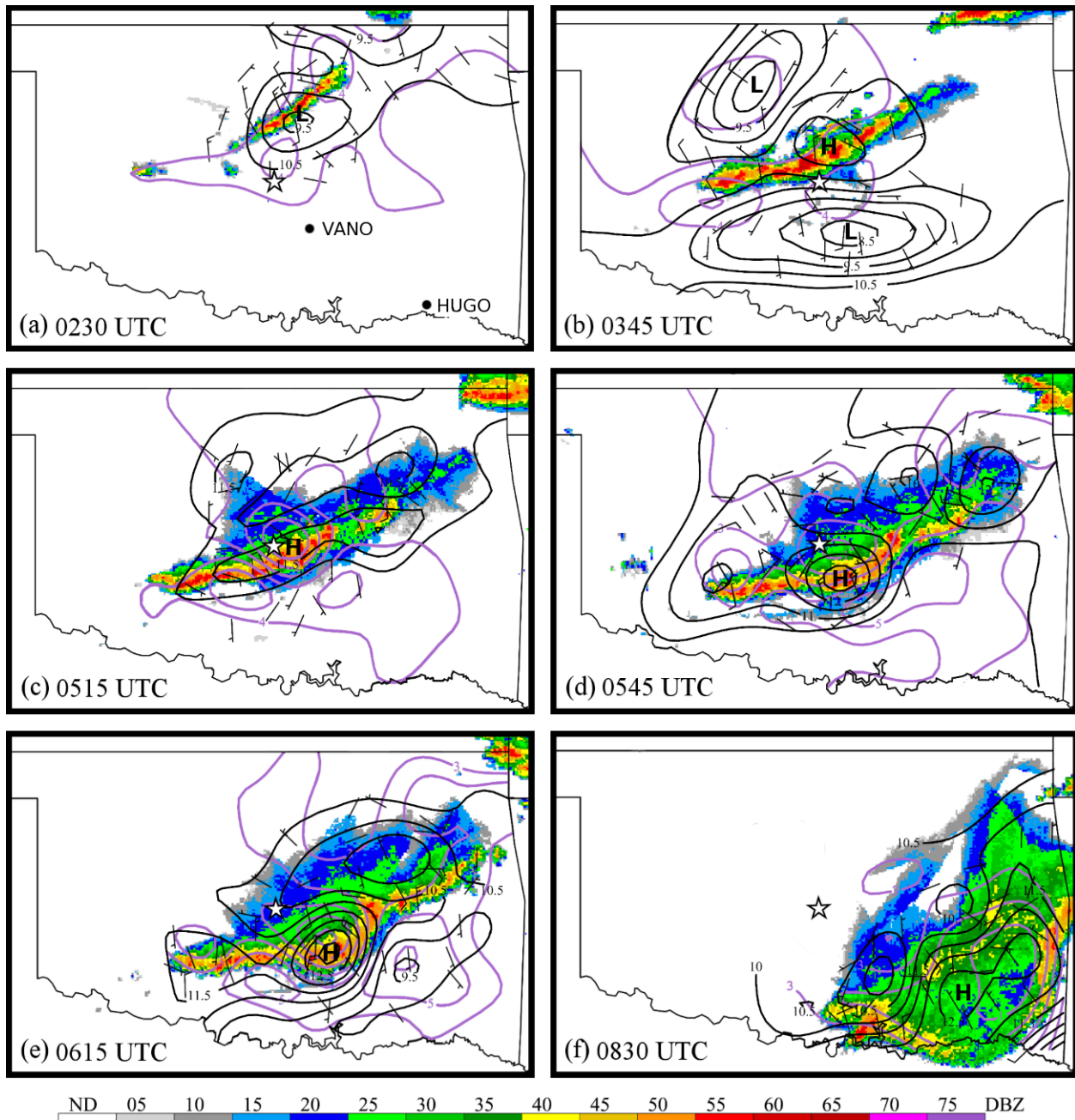


Figure 2: WSI NOWrad base reflectivity from 0230 (a), 0345 (b), 0515 (c), 0545 (d), 0615 (e), and 0830 (f) UTC 13 March 2003. High-pass filtered potential temperature (purple, 1°C), surface wind (black, barbs) and adjusted pressure (black, 0.5 hPa). High and low pressure maxima are denoted by “H” and “L” respectively. The star is the KTLX radar, and the black dots in (a) are Oklahoma mesonet stations VANO and HUGO. (From ASJ10.)

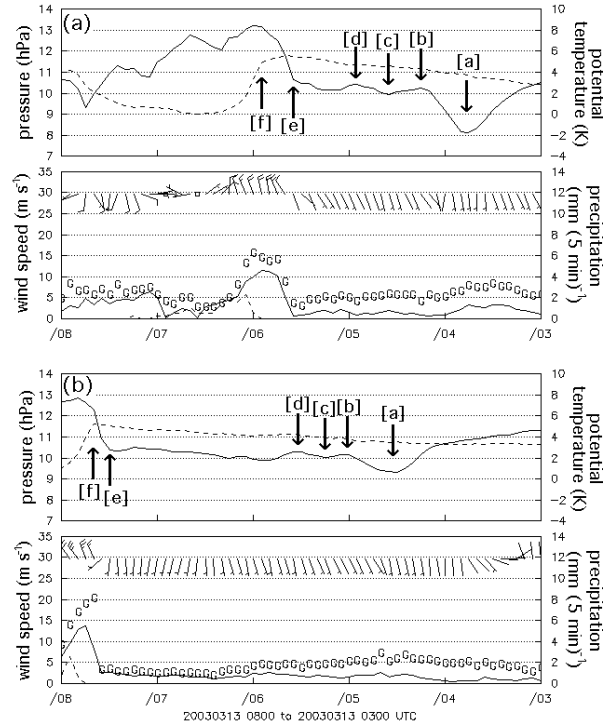


Figure 3: Timeseries display of high-pass filtered data from stations VANO (a) and HUGO (b) from the Oklahoma Mesonet (locations shown in Fig. 2a). Time increases to the left from 0300 to 0800 UTC 13 March 2003. Upper graphs in each figure show potential temperature (K, dashed, upper right scale) and adjusted pressure (hPa, solid line, upper left scale). Lower graphs show sustained winds (knots, barbs), sustained wind speed (m s^{-1} , solid line, lower left scale), unfiltered wind gusts (m s^{-1} , G, lower left scale), and unfiltered precipitation rate (mm (5 min)^{-1} , dashed line, lower right scale). [a] - [f] refer to indications of passing gravity waves or gravity current at each station and are referenced in the text.

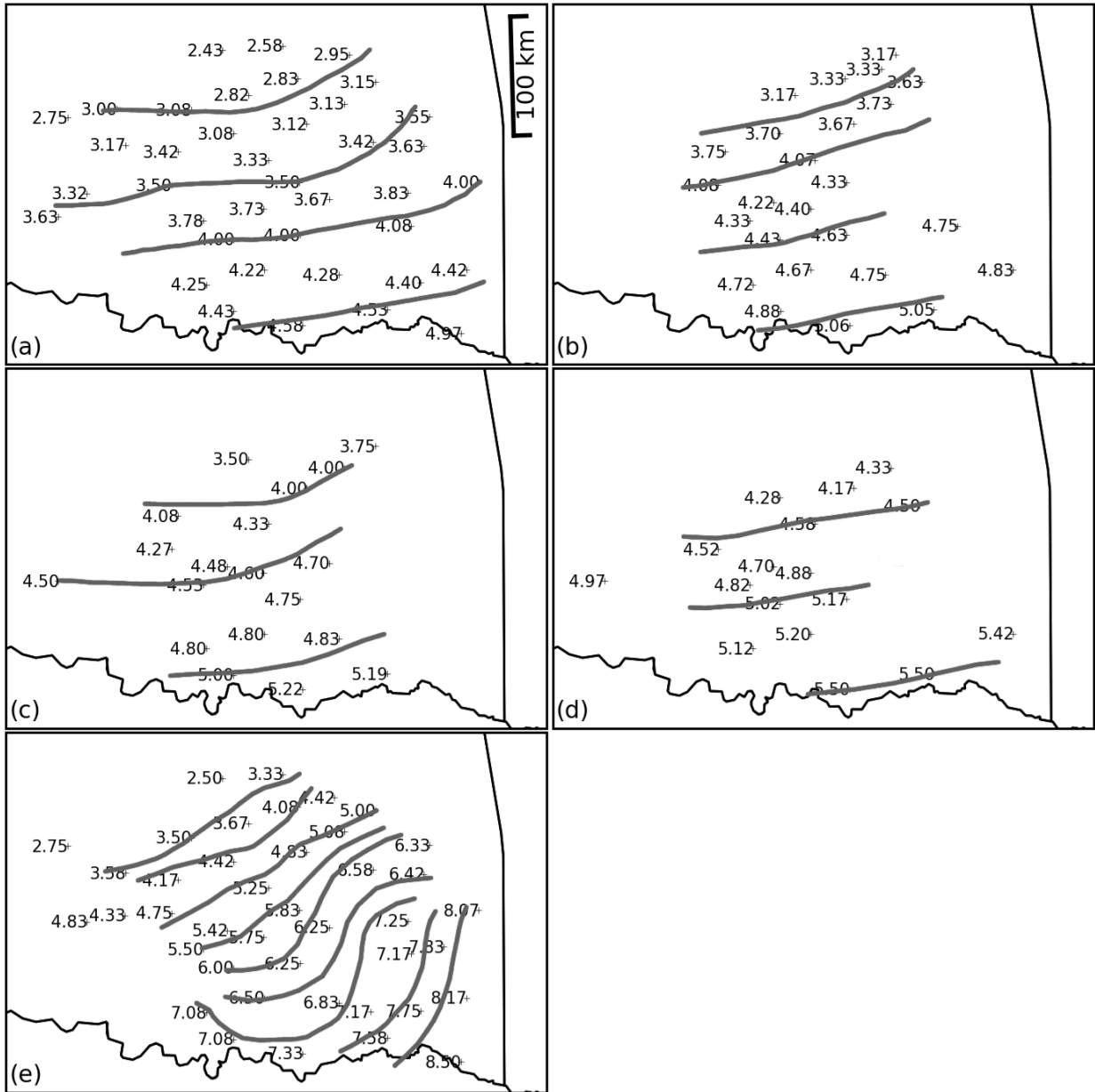


Figure 4: Isochrones (grey, contoured every 30 min) for the features noted in Fig. 3 at arrows [a], [b], [c], [d], and [e], corresponding to figure (a), (b), (c), (d), and (e), here, respectively. Only stations where each feature was observed are included (some stations are omitted for display clarity). Times are displayed in decimal format (e.g., 4.33 is 0420 UTC 13 March 2003).

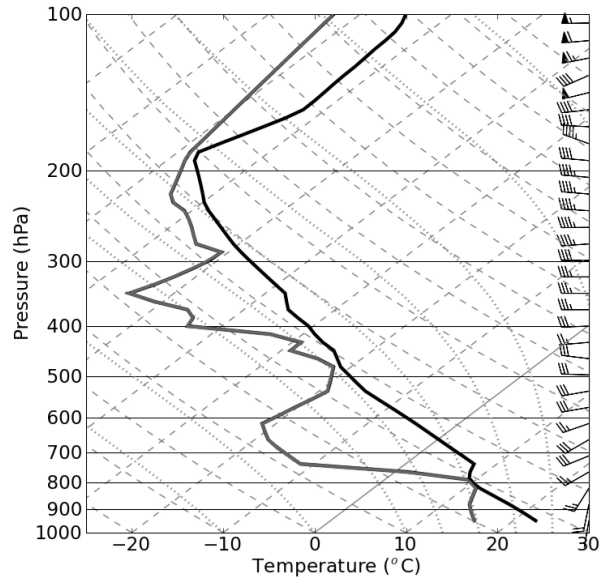


Figure 5: 0000 UTC 13 March 2003 KOUN sounding, with temperature (black, °C) and dewpoint (gray, °C).

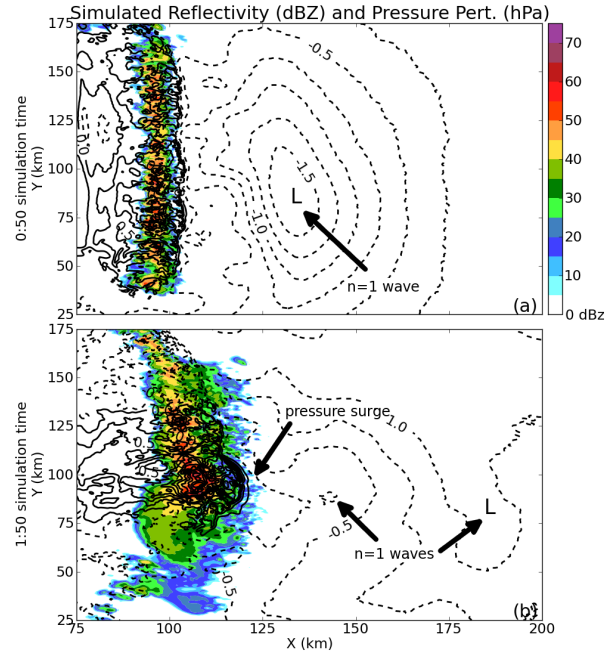


Figure 6: Simulated reflectivity (filled contours, dBZ) and pressure perturbation (black, 0.25 hPa, negative dashed) at the lowest staggered model level, 50 m, for (a) 0:50 and (b) 1:50 simulation time. Black arrows point to the $n=1$ waves and pressure surge discussed in Sections 4 and 5, respectively.

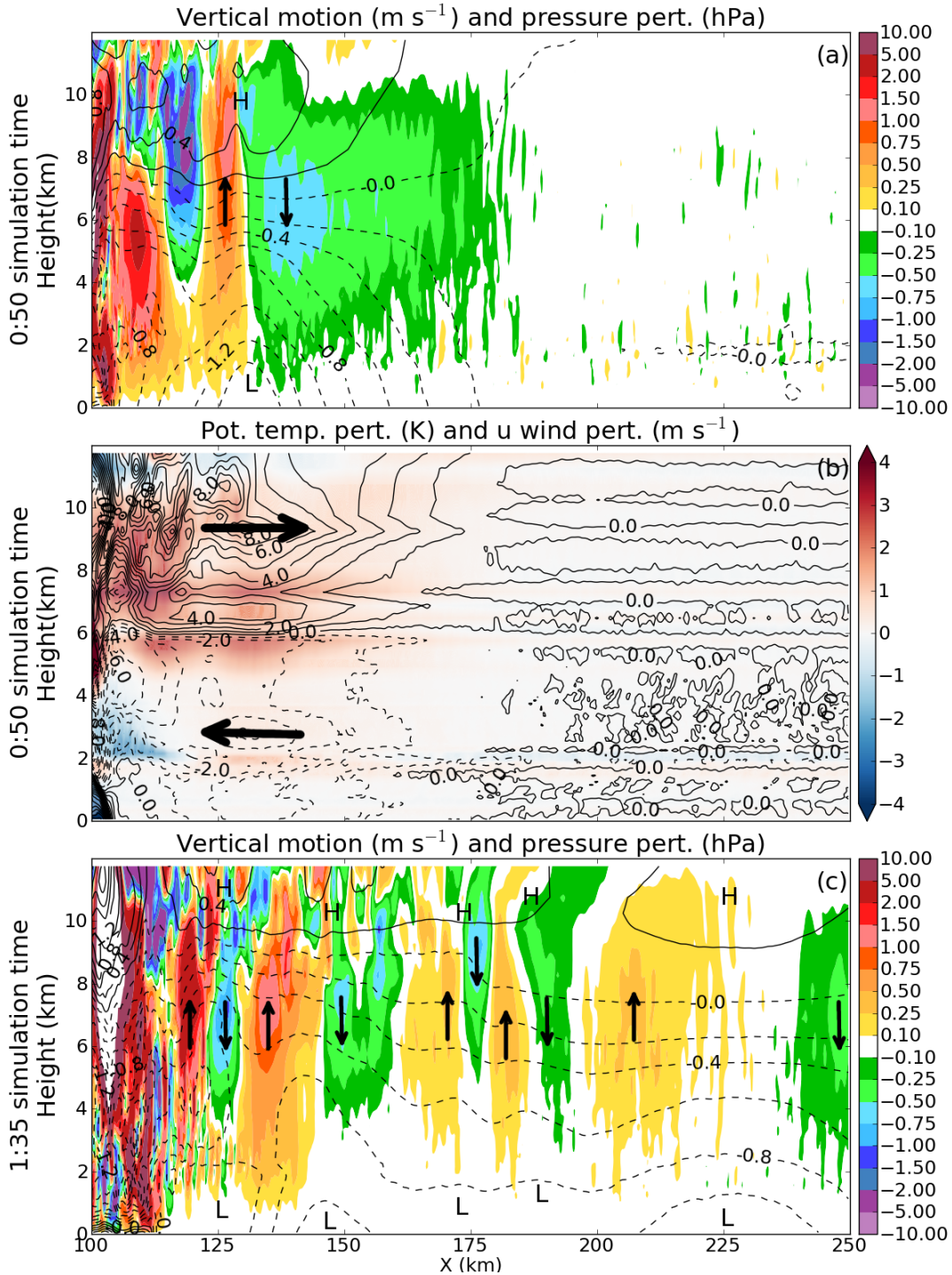


Figure 7: Vertical x cross-sections from 0-12 km, through the low pressure anomaly, averaged 5 km about the x cross-section ($y=100.5$ to 105.5 km). (a) Vertical wind speed (color, m s^{-1}) and pressure perturbation (black, 0.2 hPa, negative dashed) at 0:50 simulation time. Upward and downward motion indicated by arrows; high and low pressure perturbations by “H” and “L”. (b) Potential temperature perturbation (color, K) and u wind perturbation (black, 1 m s^{-1} , negative dashed) at 0:50 simulation time. Inflow and outflow indicated by arrows. (c) As in (a), but for 1:35 simulation time. The wave in (a), and the rightmost wave in (c), are the same feature.

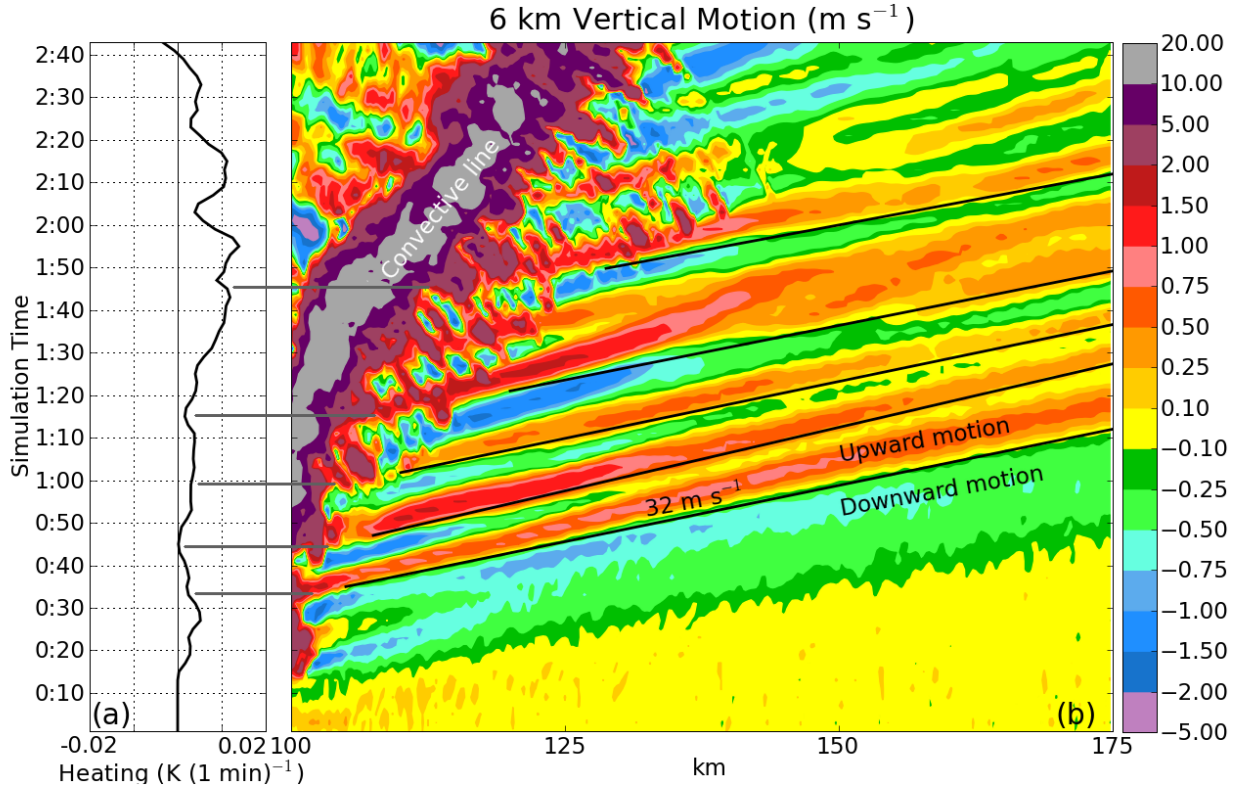


Figure 8: (a) Mean microphysical heating (K (1 min)^{-1}) between 5.2 and 7.3 km aloft, $y=100.5$ to 105.5 km as in Fig. 7, and across the entire domain in the x direction, from 0:00 to 3:00 simulation time. (b) Time evolution of horizontal distribution of vertical motion (m s^{-1}) at 6 km aloft, averaged 5 km about the x cross-section. Signature of the five gravity waves discussed in Section 4, and shown in Fig. 7c, are denoted by black lines. Grey lines connect the time of initial generation of these waves to the heating rate at the same time.

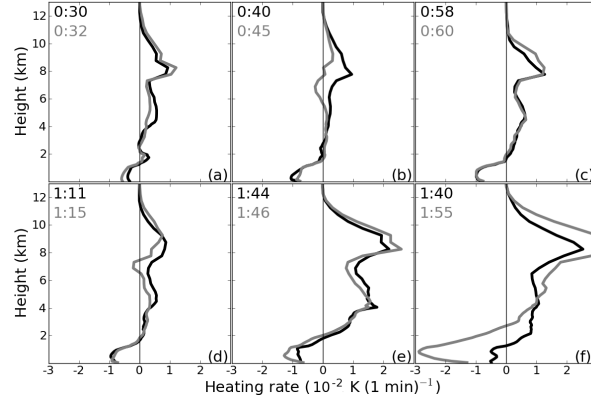


Figure 9: Mean microphysical heating profiles ($1 \times 10^{-2} \text{ K (1 min)}^{-1}$) between $y=100.5$ to 105.5 km (5 km about pressure surge) and across the entire domain in the x direction. Grey lines in (a-e) show the heating profile at the time of wave generation (waves shown in Fig. 8), black lines are the profiles from shortly before generation. (f) shows the heating profiles shortly before (black) and at the time of (grey) development of the pressure surge gravity wave. Times of each profile are noted in each subfigure.

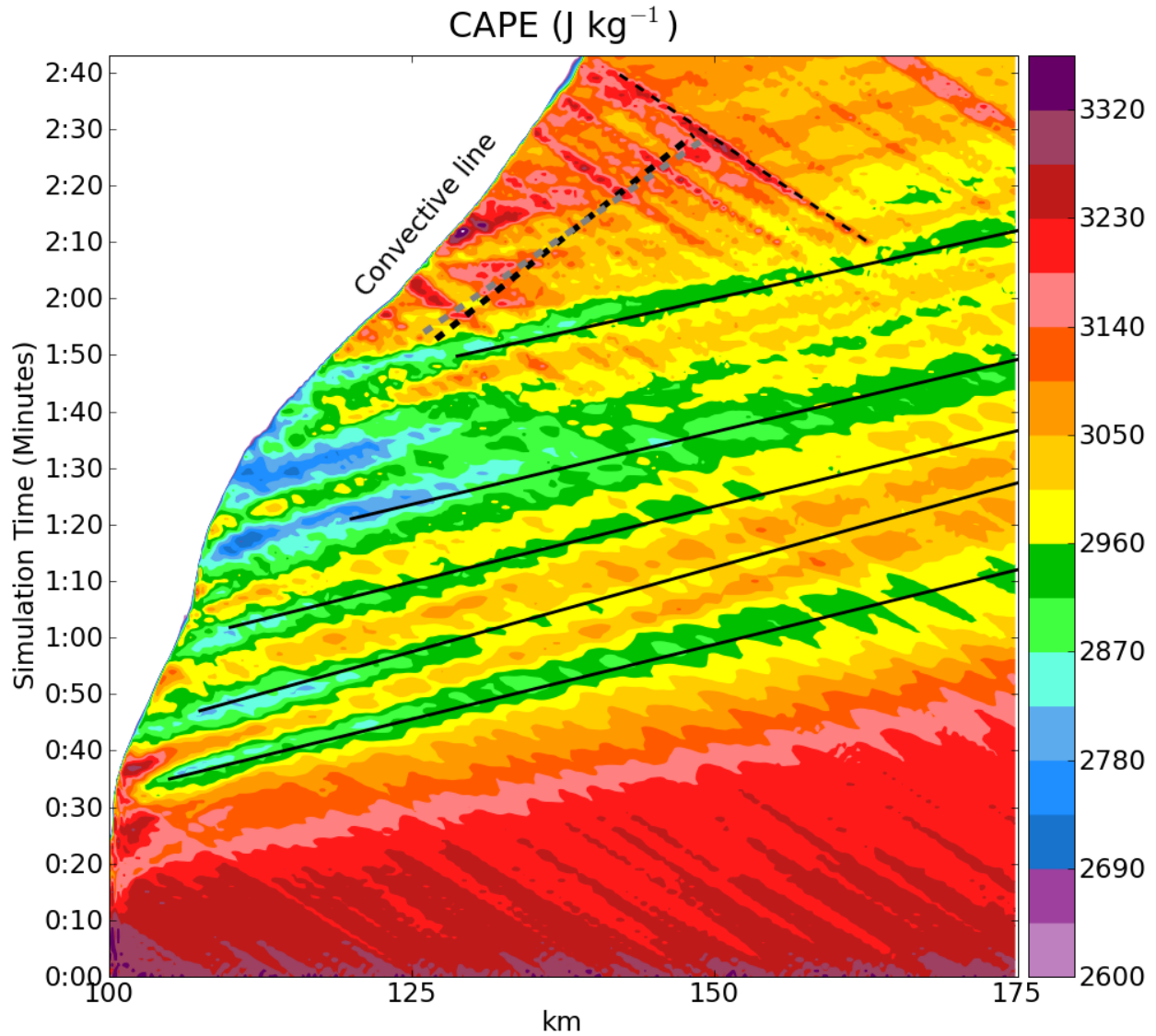


Figure 10: Time evolution of horizontal distribution of CAPE (color, 45 J kg^{-1}), averaged 5 km about the x cross-section as in Fig. 8b. Five thin black lines track the five gravity waves discussed in Section 4 and shown in Fig. 7. Thick dashed grey and black lines denote the pressure surge discussed in Section 5. Thin dashed black line tracks a cloud generated by a high-frequency gravity wave, discussed in Section 6.

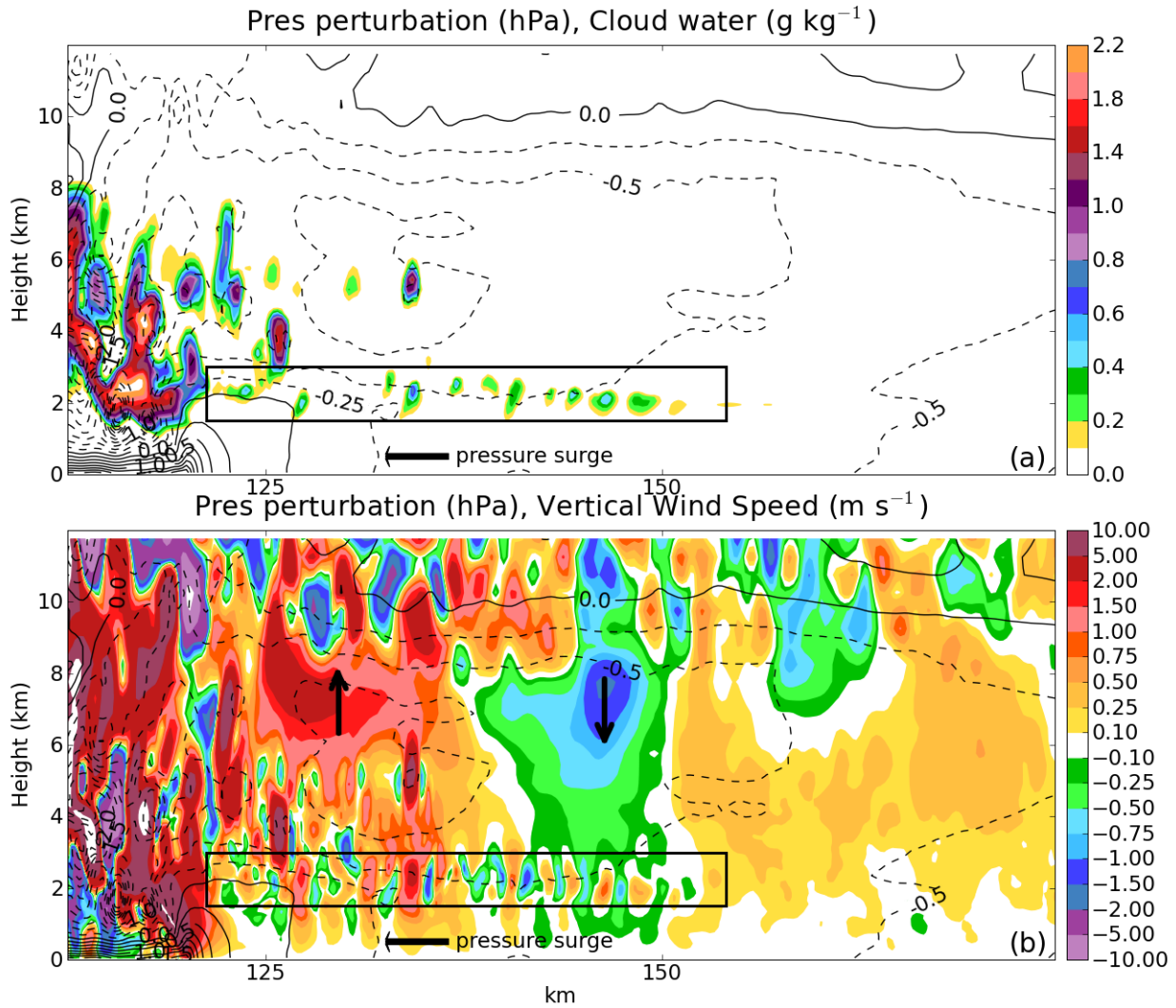


Figure 11: Vertical 0-12 km x cross-section through pressure surge, averaged 5 km about the x axis at time of surge development, 1:55 simulation time. (a) Cloud water mixing ratio (color, 0.1 g kg^{-1}) and pressure perturbation (black, 0.25 hPa , negative dashed). (b) Vertical wind speed (color, m s^{-1}) and surface pressure perturbation (as in (a)). Convective line is at approximately $x=120 \text{ km}$. The pressure surge is labelled. The vertical black arrows mark upward and downward motion. The black boxes outline the high-frequency wave signatures discussed in Section 6.

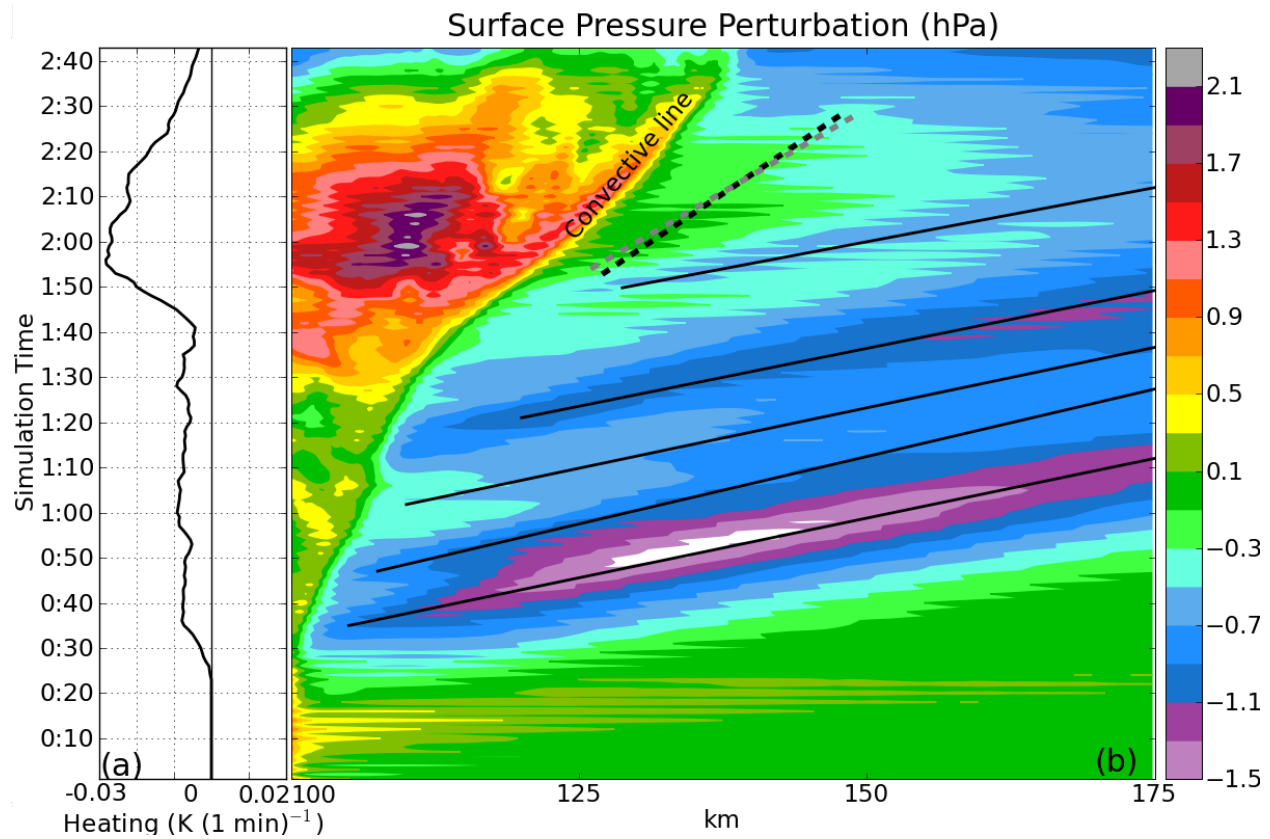


Figure 12: (a) Mean microphysical heating (K (1 min)^{-1}) between 0.65 and 1.05 km aloft, $y=100.5$ to 105.5 km (5 km about pressure surge), and across the entire domain in the x -direction. (b) Time evolution of surface pressure perturbation (hPa) averaged 5 km about the x cross-section. Thin black lines are as in Fig. 8b. The thick dashed black and grey lines show the progression of the pressure surge feature.

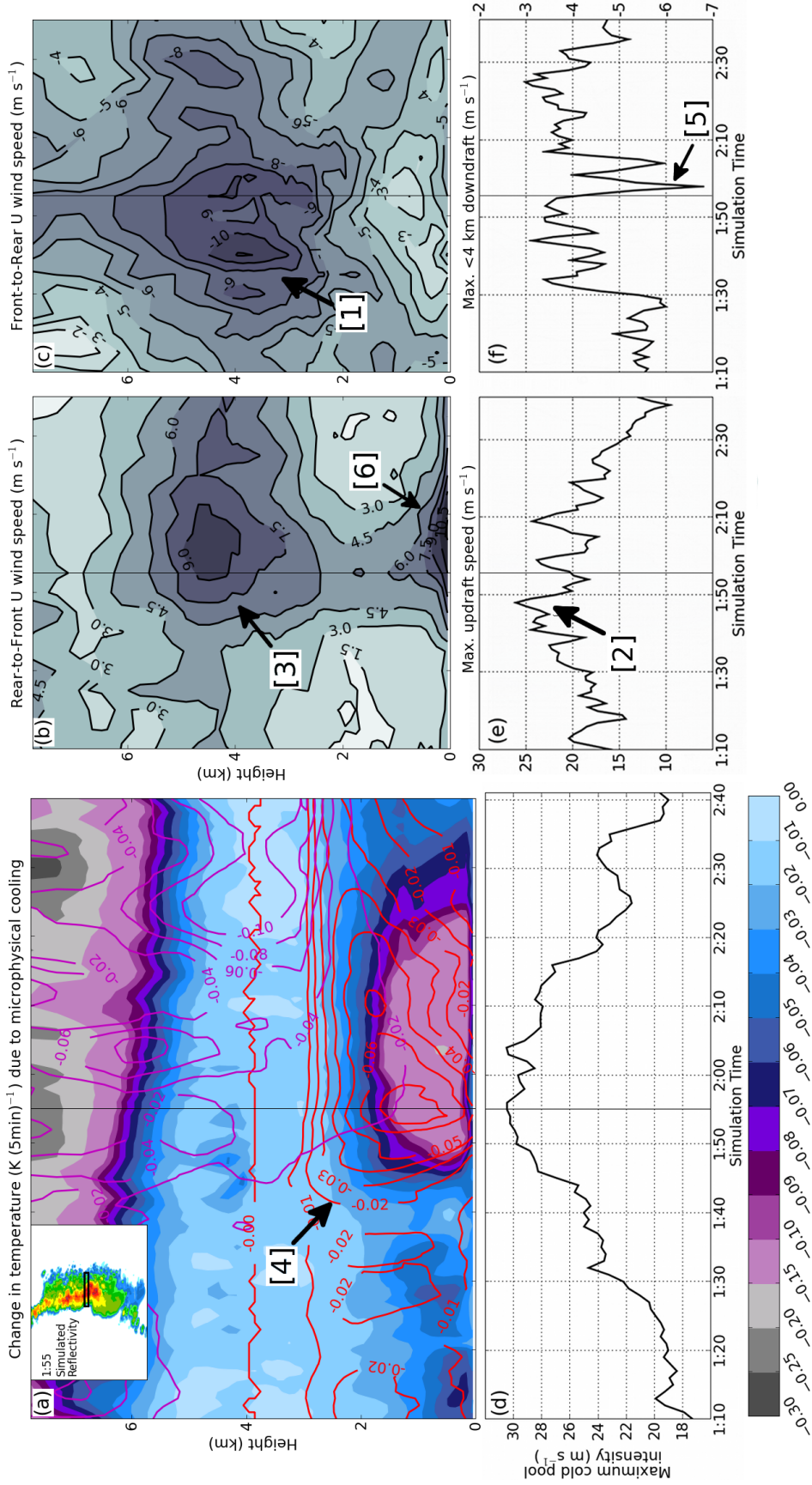


Figure 13: Time-height series of mean vertical profiles, created by averaging over the horizontal width of the system and pressure surge in the x-direction, and 5 km about the pressure surge and bow echo in the y-direction. Area averaged over shown in inset in (a); area moves with convective line. The positive and negative u wind averages were calculated separately. The thin black vertical line in each is the time of the start of the pressure surge. (a) Microphysical cooling rates due to evaporation (filled contours, K (5 min)⁻¹), melting (red, 0.01 K (5 min)⁻¹), and sublimation (purple, 0.02 K (5 min)⁻¹). (b) Storm-relative rear-to-front u wind (1.5 m s⁻¹). (c) Storm-relative front-to-rear u wind (1 m s⁻¹). (d) Maximum cold pool intensity (C, m s⁻¹). (e) Maximum upward vertical motion (1 m s⁻¹). (f) Maximum downward vertical motion (1.0 m s⁻¹). Labels [1] through [6] detail the bowing process and are discussed in the text.

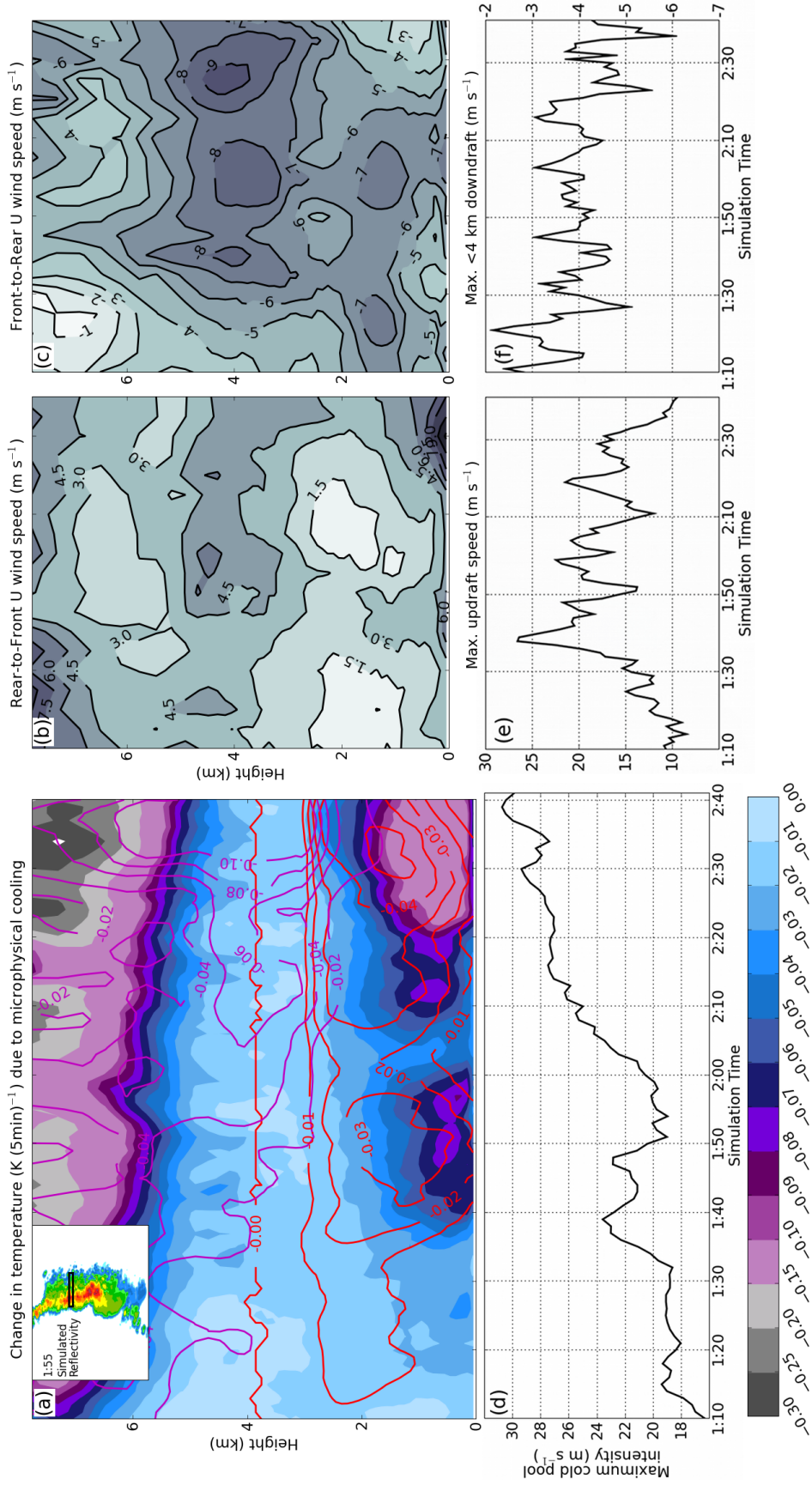


Figure 14: As in Fig. 13, but for a non-bowing segment of the convective line, shown in inset in (a).

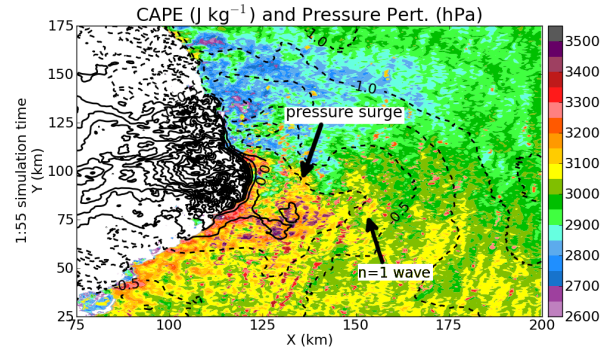


Figure 15: CAPE (J kg^{-1}) and pressure perturbation (black, 0.25 hPa, negative dashed) at 1:55 simulation time. Black arrows point to the $n=1$ wave and pressure surge discussed in Section 5.

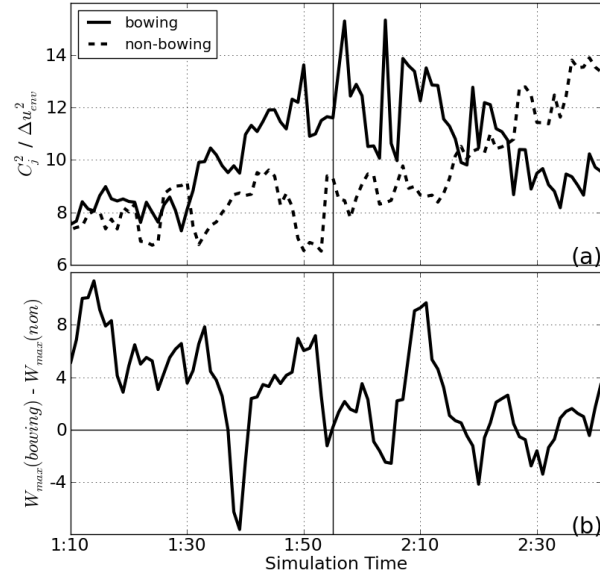


Figure 16: (a) $C_j^2 / \Delta u_{env}^2$ for cross-sections through the pressure surge and bowing convective line (solid) and through $y=125$ km, a non-bowing segment of the convective line (dashed). (b) Difference between maximum convective updraft in the bowing and non-bowing segments of the convective line. Thin black vertical line in both indicates time pressure surge first appeared ahead of the convective line.

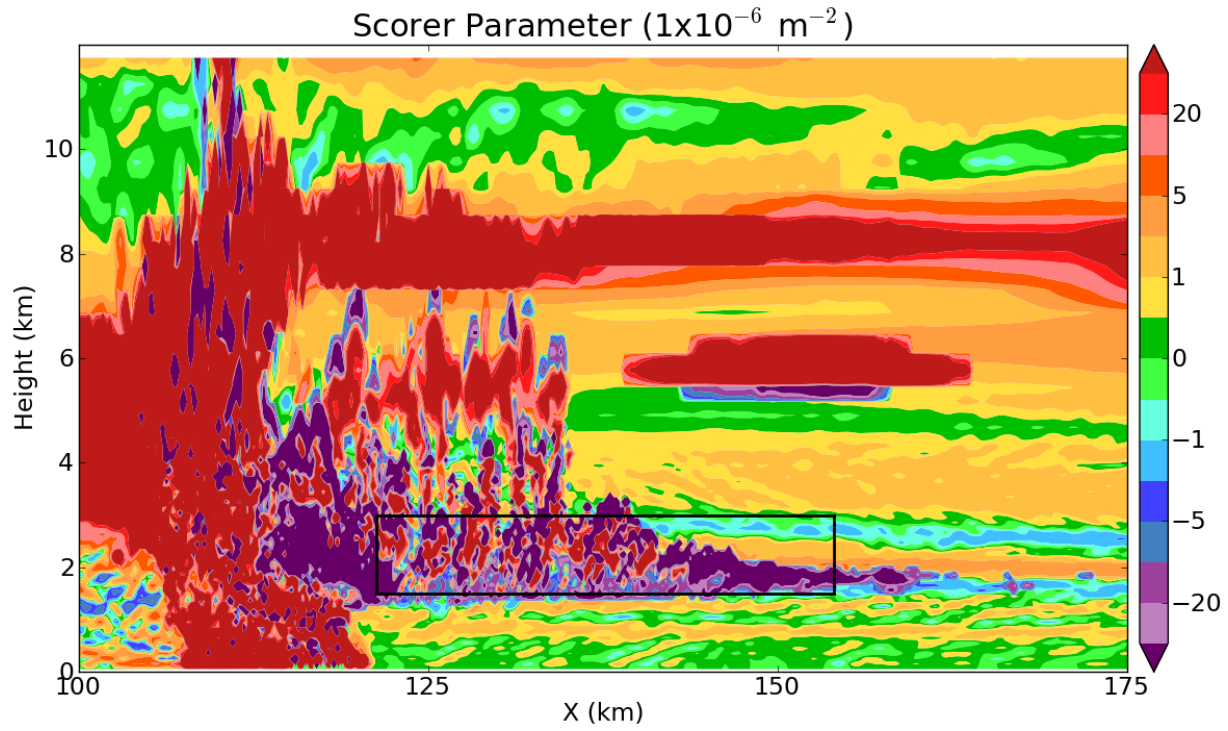


Figure 17: Vertical 0-12 km cross-section at 1:55 simulation time as in Fig. 11 of the Scorer parameter (color, $1 \times 10^{-6} \text{ m}^{-2}$) for a wave speed of 6.5 m s^{-1} . Black box delineates the same area as in Fig. 11.